frontiers | Frontiers in Earth Science

ORIGINAL RESEARCH
published: 22 June 2022
doi: 10.3389/feart.2022.824930

Depositional Controls on Detrital Zircon Provenance: An Example From Upper Cretaceous Strata, Southern Patagonia

Stephen C. Dobbs[1], Matthew A. Malkowski[2], Theresa M. Schwartz[3], Zachary T. Sickmann[4] and Stephan A. Graham[1]*

[1]Department of Geological Sciences, Stanford University, Stanford, CA, United States, [2]Department of Geological Sciences, Jackson School of Geosciences, The University of Texas at Austin, Austin, TX, United States, [3]U.S. Geological Survey, Geosciences and Environmental Change Science Center, Denver, CO, United States, [4]Institute for Geophysics, Jackson School of Geosciences, University of Texas at Austin, Austin, TX, United States

Understanding how depositional environments within a sedimentary system redistribute and sequester sediment is critical for interpreting basin-scale provenance trends. However, sedimentary source-to-sink models commonly examine temporal changes and do not consider how variation in sedimentation processes across a dispersal pathway may result in contrasting provenance signatures. In this paper, we demonstrate a down-paleoslope shift in detrital zircon provenance signatures correlated with shallow-marine lithofacies patterns from the Upper Cretaceous La Anita Formation and underlying continental slope lithofacies of the Alta Vista Formation (Magallanes-Austral Basin, southern Patagonia). New stratigraphic, sedimentologic, and lithofacies analysis results from the La Anita Formation suggest an upward shoaling succession, from a 1) storm-influenced shoreface, 2) fluvially dominated, wave-influenced delta, and a 3) high-energy, gravelly foreshore. Stratigraphic sections are paired with U-Pb detrital zircon sandstone samples (N = 20; n = 5,219), which provide both maximum depositional ages and provenance characteristics. While all samples contain abundant zircon derived from the Andean volcanic arc (ca. 145–75 Ma), the amount from both Jurassic distal volcanic massifs (ca. 188–162 Ma) and recycled orogenic sources exhumed during the advance of the Cretaceous fold-and-thrust belt (>200 Ma; 157–142 Ma) vary with changes in depositional environment. We argue that down-paleoslope, systematic enriching of local fold-and-thrust belt material within the La Anita Formation is reflective of progressive mixing of grains transported via shallow-marine processes, while distally enriched fluvio-deltaic transported zircons were sourced from large, regional catchments. This suggests that competition between transport processes across a shallow and marginal marine sequence of rocks affects the resulting provenance signatures recorded within a single stratigraphic succession. These data also detail the degree of sediment pathway connectivity between shallow-marine sources and deep-marine sinks. Detrital zircon results from muddy continental slope facies of the Alta Vista Formation are made up entirely locally derived material, while zircon results from deep-water, sand-rich channel facies of the Formation are

OPEN ACCESS

Edited by:
Claudia Ines Galli,
CONICET Instituto de Ecorregiones Andinas (INECOA), Argentina

Reviewed by:
Matias Ghiglione,
University of Buenos Aires, Argentina
Maximiliano Naipauer,
CONICET, UBA, INGEIS, Argentina

****Correspondence:***
Stephen C. Dobbs
scdobbs@stanford.edu

Specialty section:
This article was submitted to Sedimentology, Stratigraphy and Diagenesis, a section of the journal Frontiers in Earth Science

Received: *29 November 2021*
Accepted: *28 April 2022*
Published: *22 June 2022*

Citation:
Dobbs SC, Malkowski MA, Schwartz TM, Sickmann ZT and Graham SA (2022) Depositional Controls on Detrital Zircon Provenance: An Example From Upper Cretaceous Strata, Southern Patagonia. Front. Earth Sci. 10:824930. doi: 10.3389/feart.2022.824930

indistinguishable from coeval fluvio-deltaic zircon signatures. This implies that continental shelf-to-slope connectivity in a sediment dispersal system, via submarine canyons or shelf-edge delta progradation, is necessary for detrital zircon distributions from the shallow-marine realm to propagate into the deeper marine.

Keywords: detrital zircon, provenance, Patagonia, shallow marine, Cretaceous

1 INTRODUCTION

Provenance analysis of modern and ancient sediment is one of the most powerful tools for decoding signals of evolution—be it tectonic, environmental, geographic, or otherwise—within a source-to-sink sedimentary system. Detrital zircon studies are now commonly used in basin analysis, wherein zircon analysis is paired with stratigraphic (e.g., Dickinson and Gehrels, 2009), sedimentological (e.g., Garzanti et al., 2009; Schwartz et al., 2017; Leary et al., 2020), geochemical (e.g., DeCelles et al., 2004; Malkowski et al., 2019), tectonic (e.g., Finzel et al., 2015; Gooley et al., 2021) and paleogeographic (e.g., Cawood et al.,

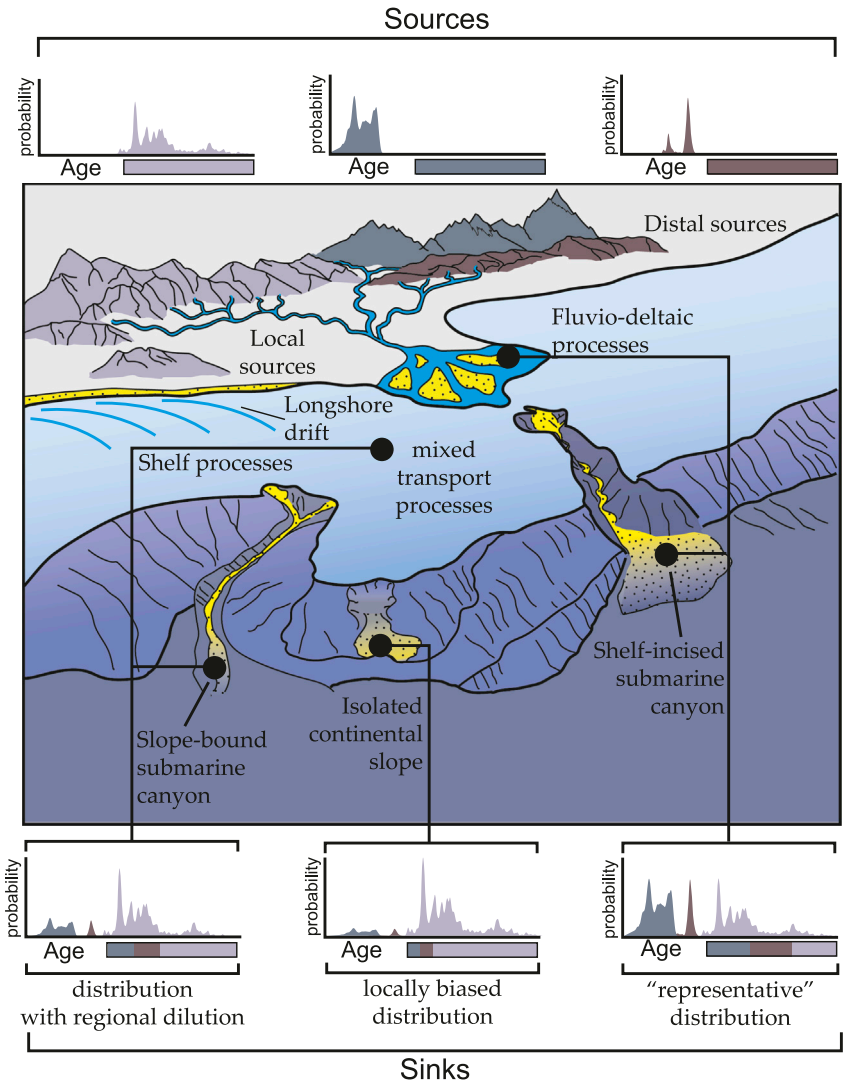

FIGURE 1 | Schematic illustration of a fictional source-to-sink model and resultant detrital zircon age distributions across different depositional environments. Sources are represented by different onshore watersheds with varying detrital zircon age distributions. The down-slope sinks represent the possible shifts in provenance spectra caused by the interplay of several transport and erosion processes. Note that while a shelf-connected submarine canyon system may have a similar spectrum to its fluvio-deltaic sources that are able to provide distally derived sediments, disconnected portions of the shelf and slope may record disparate age signals that are biased by local sources.

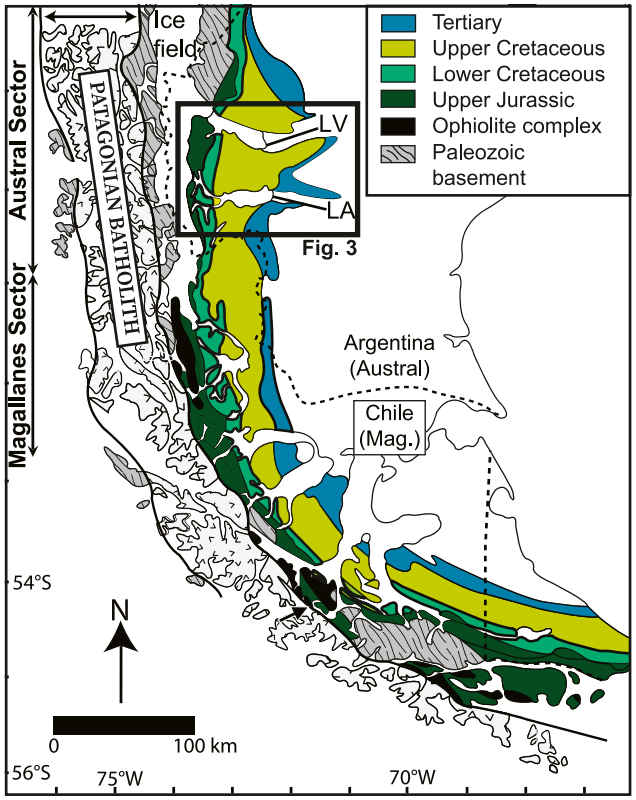

FIGURE 2 | (A) Overview geologic map of the Jurassic through Cenozoic outcrop belt of the Magallanes-Austral Basin in southern South America modified from Malkowski et al. (2017a). LA, Lago Argentino; LV, Lago Viedma; Mag, Magallanes. Dashed line is the Chile (Magallanes sector)-Argentina (Austral basin sector) boundary. Black rectangle outlines location of **Figure 3**.

2007; Sharman et al., 2015) studies in order to better constrain spatiotemporal evolutions of provenance signals. However, the interpretation that detrital zircon analyses yield reliable provenance records relies on an *a priori* assumption that sandstone samples represent a homogenized signature of the relative contributions from all source areas. If one is to interpret inter-sample variation in zircon signal strength as geologically significant, then reasonable effort should be made to ensure biasing mechanisms such as hydrodynamic fractionation of zircon (e.g., Lawrence et al., 2011; Ibañez-Mejia et al., 2018; Leary et al., 2020; Cantine et al., 2021), variation in zircon host-rock fertility (e.g., Moecher and Samson, 2006), dilution or propagation of zircon signals down depositional gradient (e.g., Cawood et al., 2003; Malkowski et al., 2017a; Malkowski et al., 2019), and/or lithostratigraphic zircon spectra variability within a genetically related clastic succession (e.g., DeGraaff-Surpless et al., 2003) do not significantly impact detrital zircon distributions.

These complications inherent to detrital zircon provenance analysis make it difficult to assess how interactions between various transport processes across depositional environments along a source-to-sink system can affect provenance signals (**Figure 1**). DeGraaff-Surpless et al. (2003), for example, demonstrated that submarine-fan deposits from the Albian–Santonian Harts Pass Formation contained a stratigraphically heterogeneous detrital zircon spectra correlated with variation in lithofacies. Their work suggested that intraformational comparison of detrital zircon spectra is necessary to better constrain variability in provenance records.

In this paper, we first describe lithofacies associations to establish depositional context from the Upper Cretaceous La Anita Formation (southern Patagonia, Argentina). We then wed our lithofacies analysis with systematic detrital zircon sampling to assess the role depositional environments play on detrital zircon provenance trends in a well-documented progradational succession of slope, shelf, and onshore deposits. We demonstrate that detrital zircon distributions document a systematic shift in provenance trends moving down depositional gradient and propose that the progressive interaction with local shallow-marine transport processes diluted regional catchment signals recorded in fluvio-deltaic depocenters. We also compare these data to detrital zircon results from the continental slope facies from the underlying Alta Vista Formation to assess sediment pathway connectivity of shallow-marine sources to deep-water basins. This work suggests that to accurately assess the provenance history of a sedimentary succession, it may be necessary to systematically sample the successions across changes in lithofacies.

2 GEOLOGIC HISTORY

The Magallanes-Austral Basin, located in southern Patagonia (ca. 46–56° S; **Figure 2**), records the geological history of the initial breakup of the southwestern margin of the Gondwana supercontinent followed by the subsequent emplacement of the South Patagonian batholith via a two-phase basin fill marked by extensional volcanism and foreland sedimentation. Jurassic–Early Cretaceous rifting of southwestern Gondwana is signaled by the opening of the Rocas Verdes backarc basin (Dalziel et al., 1974; de Wit and Stern, 1981; Pankhurst et al., 2000; Fildani and Hessler, 2005). Crustal extension is recorded via bimodal mafic-silicic volcanic and volcaniclastic rocks of the El Quemado complex and ophiolite assemblages that floored the quasi-oceanic rift basin (Pankhurst et al., 2000; Caldéron et al., 2007; Caldéron et al., 2013). These rocks unconformably overlie Eastern Andean metamorphic basement complexes which are cut by graben structures associated with rifting (Allen, 1982; Wilson, 1991; Stern and de Wit, 2003). Late Jurassic through Early Cretaceous crustal extension produced accommodation starting from the southern terminus of the basin that propagated northward (Stern and de Wit, 2003; Malkowski et al., 2016). This "unzipping" of the continent produced a north-south extensional gradient wherein the northern portion of the basin is narrow and underlain by attenuated continental crust while the southern extent widens and is floored by oceanic crust with mid-ocean ridge basalt geochemical characteristics (de Wit and Stern, 1981; Alabaster and Storey, 1990; Stern and de Wit, 2003; Malkowski et al., 2016). The Rocas Verdes basin

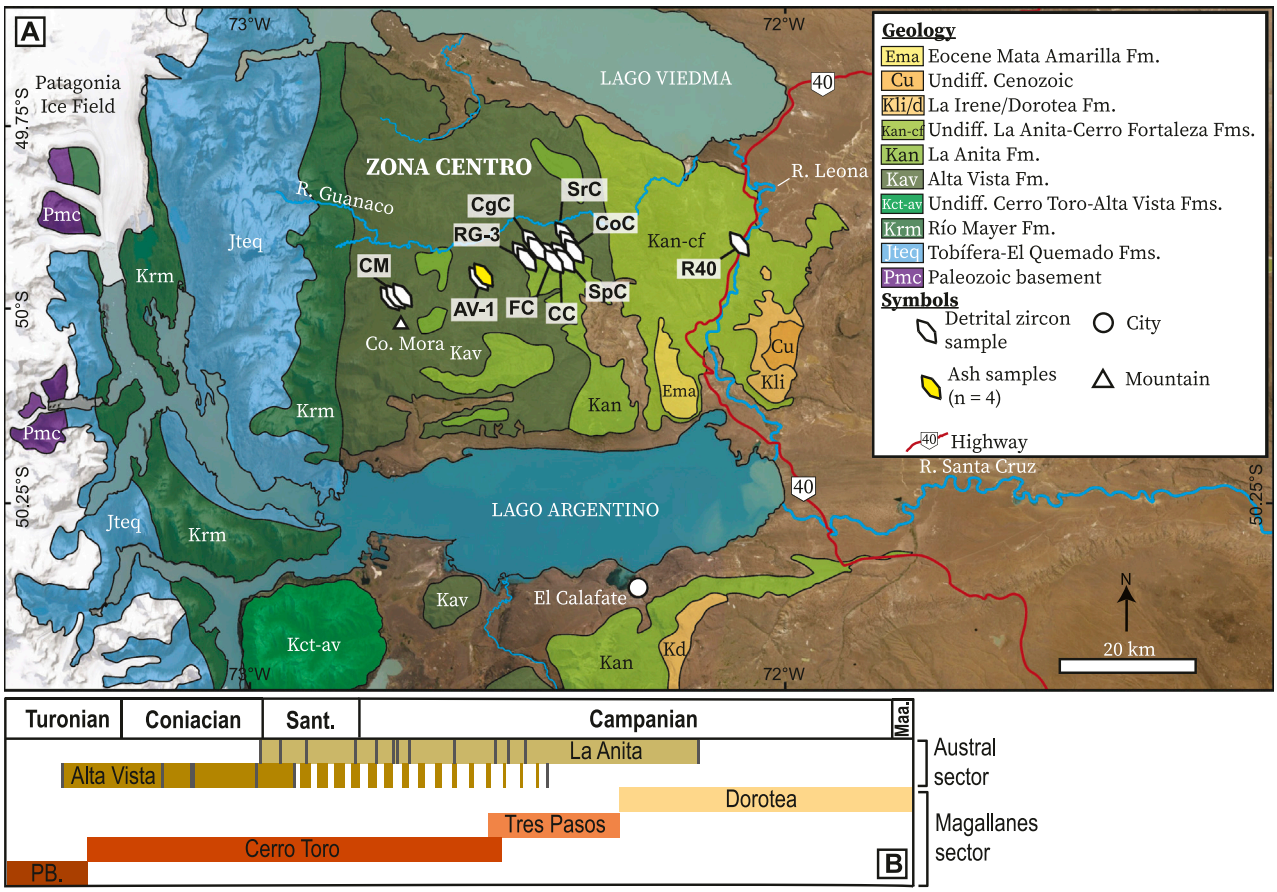

FIGURE 3 | (A) Geologic map of the Zona Centro region, modified after Ghiglione et al. (2014) and Sickmann et al. (2018); Sickmann et al. (2019). Stratigraphic sections are labeled (**Figure 4**). **(B)** Chronostratigraphic age correlation between Austral (Alta Vista and La Anita Formations) strata from this study and units from the Magallanes sector compiled by Daniels et al. (2019). Alta Vista Formation line becomes dashed as the late Santonian through Campanian age range is defined by a single middle Campanian maximum depositional age. The rest of the ash and sandstone ages range between the Turonian and Santonian for the Alta Vista Formation. Gray vertical lines on the Alta Vista and La Anita Formation rectangles highlight maximum depositional ages from individual samples. PB, Punta Barrosa Formation.

stratigraphy consists primarily of volcaniclastic rocks from the silicic El Quemado complex and Tobífera Formation, which is overlain by the shale dominated Zapata Formation (also known as the Río Mayer Formation in Argentina) (Wilson, 1991; Fildani and Hessler, 2005; Caldéron et al., 2007). Shales of the Zapata Formation have been interpreted to represent filling of the Rocas Verdes Basin from locally derived basement uplifts and juvenile calc-alkaline volcanic materials from the incipient Andean volcanic arc (Fildani and Hessler, 2005).

Increased rates of rifting of the nascent South Atlantic Ocean and subduction along the eastern Pacific margin rearranged the tectonic forcings from a net extensional to net compressional regime by the Cenomanian–Turonian (Dalziel, 1986; Ramos, 1989; Wilson, 1991; Calderón et al., 2013). Crustal shortening and the emplacement of the Andean fold-and-thrust belt inboard of the volcanic arc led to the closure of the Rocas Verdes Basin and substantial foreland subsidence, which ushered in the Magallanes-Austral foreland phase of the basin (Wilson, 1991; Fildani et al., 2003; Fildani and Hessler, 2005). Basin deepening (Natland et al., 1974) coupled with the onset of deep-water, coarse-clastic deposition into the basin from the Upper Cretaceous Punta Barrosa Formation marks the first stratigraphic response to foreland basin development (Wilson, 1991; Fildani et al., 2003; Fildani and Hessler, 2005; Malkowski et al., 2017b). However, the initiation of the foreland basin stage may have occurred in a diachronous manner, where northern foreland depocenters developed as early as the Aptian–Albian (Wilson, 1991; Fosdick et al., 2011; Ghiglione et al., 2015; Aramendía et al., 2018). The distribution of foreland sediments is thought to be strongly controlled by both predecessor basin geometries from its extensional phase and diachronous tectonostratigraphic responses to progressive basin closure in a north to south direction (Wilson, 1991; Arbe, 2002; Crane and Lowe, 2008; Hubbard et al., 2008; Romans et al., 2010; Malkowski et al., 2017a; Malkowski et al., 2017b; Malkowski et al., 2018; Sickmann et al., 2019). Deposition of the Santonian–Campanian Alta Vista and Campanian Tres Pasos Formations record continued deep-marine deposition and progradation of slope clinoforms southward in the forms of deep-water channel systems and continental slope mass-transport

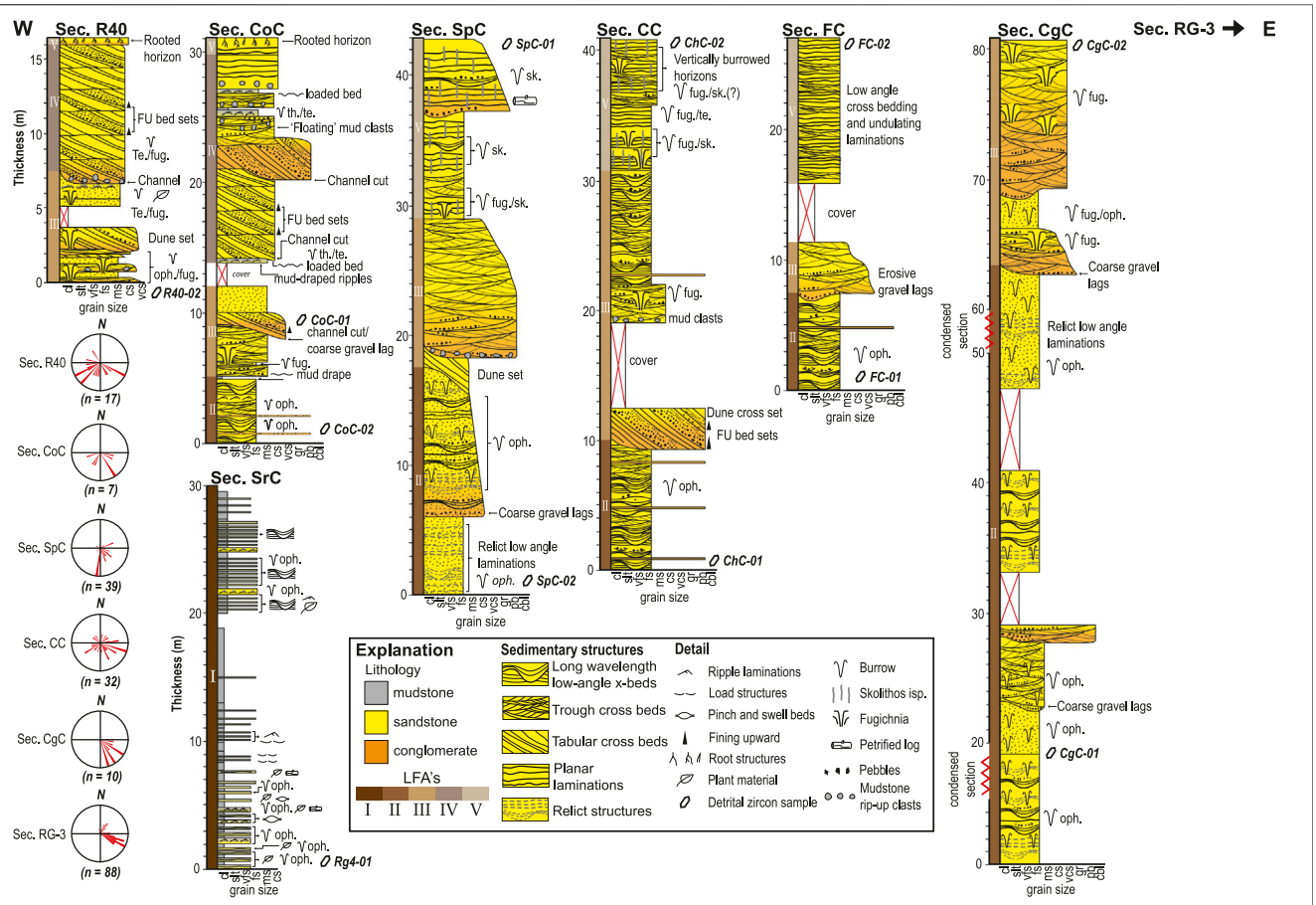

FIGURE 4 | Measured stratigraphic sections and paleocurrent results from the La Anita Formation from the Zona Centro region (**Figure 3A**). Sections are at the meter scale with grain size is on the *x*-axis (cl, clay; slt, silt; vfs, very fine sand; fs, fine sand; ms, medium sand; cs, coarse sand; vcs, very coarse sand; gr, granule; pb, pebble; cbl, cobble). Colored sections labeled with roman numerals are lithofacies associations. Homogeneous sections are condensed and signified by a red, vertical zig-zag line. A detailed stratigraphic section of section RG-3 is available in **Supplementary Figure S1**. *Fug*, fugichnia escape burrows; *Oph*, *Ophiomorpha isp.*; *Sk*, *Skolithos isp.*; *Th/Te*, *Thalassinoides/ Teredolites isp.*

deposits (Macellari at al., 1989; Arbe, 2002; Shultz et al., 2005; Armitage et al., 2009; Romans et al., 2009; Hubbard et al., 2010; Daniels et al., 2018; Sickmann et al., 2018; Sickmann et al., 2019). In the northern (Austral) portion of the basin, muddy continental slope facies of the Alta Vista Formation are overlain by shallow to marginal marine deposits of the Campanian La Anita Formation (Macellari et al., 1989; Arbe, 2002; Moyano Paz et al., 2018; Sickmann et al., 2018; Ghiglione et al., 2021).

The La Anita and Alta Vista Formations are exposed between Lago Argentino and Lago Viedma and the southeastern coast of Lago Argentino (**Figure 3**). The La Anita Formation gradationally transitions upward from muddy, mass-transport dominated continental slope facies of the Alta Vista Formation (Sickmann et al., 2018; **Figure 3A**). The stratigraphy of the La Anita Formation consists of heterolithic fine-grained sandstone and mudstone packages that shoal into coarse-grained, channelized, and cross-bedded sandstone and pebble conglomerate. Ammonite fossils constrain the age of the formation to Campanian (Riccardi and Rolleri, 1980), which has been extended to ca. 86–80 Ma via maximum depositional ages from detrital zircon geochronology (Sickmann et al., 2018; Sickmann et al., 2019; Ghiglione et al., 2021). Stratigraphic interpretations of the La Anita Formation suggest a wave- and fluvial-influenced delta system whose sediment was redistributed on the continental shelf via a combination of wave action and fluvio-deltaic progradation (Macellari et al., 1989; Arbe, 2002; Moyano Paz et al., 2018). The La Anita Formation in the study area is overlain by terrestrial deposits of the Campanian Cerro Fortaleza Formation (Sickmann et al., 2018). A regional Paleogene unconformity separates Upper Cretaceous stratigraphy from Cenozoic synorogenic deposits up to middle Miocene in age.

3 SEDIMENTOLOGY AND STRATIGRAPHY OF THE LA ANITA FORMATION

Seven stratigraphic sections were measured at the decimeter scale along an approximately 5 km long outcrop belt north of Lago Argentino (**Figures 3A**, **4**). One additional section was measured approximately 25 km east of the outcrop belt, adjacent to Ruta 40

TABLE 1 | Lithofacies and lithofacies association descriptions from the La Anita Formation.

TABLE 1A Lithofacies descriptions

Lithofacies	Color	Grain size	Bed thickness	Bed geometry	Sedimentary structures and features	Bioturbation index (BI)	Ichnospecies	Lithologic Accessories
LF1: Planar to undulating to planar laminated sandstone interbedded with mudstone	Gray to buff	Very fine to fine sandstone, mudstone, siltstone	Mean = 29 cm, 1σ = 45cm, Range = 2–380 cm	Tabular and continuous	Current ripple lamination, horizontal planar lamination, undulous lamination, micro-hummocky lamination	0–1	*Ophiomorpha isp., Rhizocorallium isp.*	Plant debris
LF2: Poorly laminated siltstone and mudstone	Gray	Siltstone and mudstone	Mean = 24 cm, 1σ = 24cm, Range = 2–175 cm	Tabular and continuous	Poorly developed planar lamination	0		Plant debris
LF3: Laminated black shale	Black and dark gray	Mudstone and claystone	Mean = 15 cm, 1σ = 32 cm, Range = 1–150 cm	Tabular and continuous or draping	Poorly developed planar laminations	0		Plant debris
LF4: Hummocky and Swaley cross-bedded sandstone	Gray to white	Very fine to fine sandstone	Mean = 28 cm, 1σ = 10 cm, Range = 20–40 cm	Pinch and swell, discontinuous	Hummocky cross stratification, current ripple lamination, horizontal planar lamination	0		
LF5: Massive thick-bedded sandstone	Gray, white, buff	Very fine to fine sandstone	Mean = 58cm, 1σ = 69 cm, Range = 5–440 cm	Tabular, laterally continuous	Swaley cross stratification, current ripple lamination, horizontal planar lamination, soft-sediment deformation	4–6	*Ophiomorpha isp.*	Coarse gravel lags, plant debris, isolated quartzite pebbles and cobbles
LF6: Trough cross bedded sandstone	White to buff	Medium lower to very coarse sandstone	Mean = 48 cm, 1σ = 72 cm, Range = 5–360 cm	Tabular and continuous or channelized	Trough and planar cross bedding, current ripple laminations, gravel oscillation ripples	0–3	*Ophiomorpha isp., Rosselia isp., Skolithos isp.*	Coarse gravel lags, Fugichnia escape structures, mudstone rip-up clasts, isolated quartzite pebbles and cobbles
LF7: Cross bedded sandstones with gravel lenses	Buff	Medium to very coarse sandstone	Mean = 31 cm, 1σ = 23 cm, Range = 10–120 cm	Channelized, erosive or tabular	Trough cross bedding, mudstone rip up clasts, fining upward cross sets, gravel lenses, escape burrows, soft-sediment deformation	0–2		Coarse gravel lags, Fugichnia escape structures, mudstone rip-up clasts
LF8: Massive coarse-grained sandstone and tabular cross bedded sandstone	Buff	Coarse to very coarse sandstone	Meter scale (ca. ~2 m)	Channelized, erosive	Massive, fining upward beds, soft-sediment deformation	0		Mudstone rip-up clasts, petrified logs
LF9: Thin-bedded ripped sandstone	White to gray	Very fine to fine sandstone	Sandstone bed sets ca. 50 cm thick. Lamina-scale contain interstratified mud drapes	Discontinuous, pinch and swell away from channel features	Current ripple lamination, mud-draped ripples, planar and undulous lamination, soft-sediment deformation	0–2	*Thalassinoides isp., Teredolites isp.*	

(Continued on following page)

TABLE 1 | (*Continued*) Lithofacies and lithofacies association descriptions from the La Anita Formation.

TABLE 1A Lithofacies descriptions

Lithofacies	Color	Grain size	Bed thickness	Bed geometry	Sedimentary structures and features	Bioturbation index (BI)	Ichnospecies	Lithologic Accessories
LF10: Carbonaceous mudstone	Black	Clay to silt	Beds ca. 1–10 cm thick	Tabular, although commonly eroded into via overlying loading	Planar lamination, soft-sediment deformation	0–2	*Thalassinoides isp.*	Plant debris
LF11: Planar to cross bedded sandstone	Brown to desert-varnished purple	Fine to very coarse sandstone	Beds ca. 5–15 cm thick	Tabular	Weak planar lamination, planar cross bedding	0–3	*Skolithos isp.*	Petrified logs, dinosaur bones, fugichnia escape structures, isolated pebbles and cobbles
LF12: Planar bedded to cross-bedded pebble conglomerate	Brown to desert-varnished purple	Pebble to cobble conglomerate	Beds ca. 5–10 cm thick	Tabular	'Pancake'-like bedding possibly preserving relict planar lamination, planar cross bedding	0		Petrified logs, dinosaur bones

TABLE 1B Lithofacies Associations

Lithofacies Associations	Lithofacies	Sedimentary characteristics	Approximate thickness	Ichnospecies assemblage	Depositional environment
LFA-1	1–4	Interbedded heterolithic deposits of vf to f. sandstone and silt/mudstones. Thin-bedded and mud dominated. Current ripple lamination, planar lamination, and low angle, long wavelength cross bedding interpreted as HCS.	Exposed thickness of ca. 50 m	*Ophiomorpha isp., Rhizocorallium isp.;* BI = 0–2	Wave and storm influenced lower shoreface and inner shelf. Below fair-weather wave base. Transport accommodated primarily by storm-generated currents.
LFA-2	2, 4–5	Pervasively bioturbated, amalgamated vf to f sandstone sporadically interbedded with silt/mudstone. Low angle cross bedding reminiscent of Swaley cross strata with isolated coarse gravel lags common up section	Approximately 70 m maximum thickness	*Ophiomorpha isp.;* BI = 4–6	Wave and storm influenced lower to middle shoreface. Between storm and fair-weather wave base. Advantageous for burrowing species, suggesting periods of quiescence.
LFA-3	1–2, 6–7	mL to vc cross bedded sandstone interbedded subordinately with thin-bedded rippled sandstones and siltstones	Maximum thickness ca. 15 m	*Rosselia isp., Ophiomorpha isp., Skolithos isp., fugichnia*; BI = 0–3	Upper shoreface consisting of dune-scale trough cross bedded sandstones and conglomerates. High-energy, coarse-grained shoreface deposited above fair-weather wave base via shoaling wave energy, longshore drift, rip currents and/or geostrophic flows.
LFA-4	1–2, 6–10	mL to vc cross bedded amalgamated to cross bedded, fining upward sandstones and pebble conglomerates with subordinate amounts of fine-grained planar to ripple laminated sandstone and carbonaceous mudstone	Maximum thickness ca. 20 m	*Rosselia isp., Ophiomorpha isp., Skolithos isp., Thalassinoides isp., Teredolites isp., Arenicolites(?) isp., fugichnia*; BI = 0–2	Delta plain interdistributary (terminal?) channels and mouth bars/levees. River dominated. Both single and multi-story with high sedimentation rates.
LFA-5	11–12	fine to cU sandstone and pebble conglomerate with relict undulous to planar lamination. Petrified logs, dinosaur bones, and root structures common.	Maximum thickness ca. 10 m	*Skolithos isp., fugichnia,* root structures	High energy foreshore near the interface between marine and terrestrial deposition. Possible beach deposits in zones of relict planar lamination.

(**Figures 3A**, **4**). In total, we present an analysis of ~400 m of strata from the La Anita Formation in order to assess vertical and lateral variations across the formation. We also present descriptions from two stratigraphic sections from continental slope facies of the underlying Alta Vista Formation (sections AV-1 and CM; **Figure 3A**). Stratigraphic sections were divided into 12

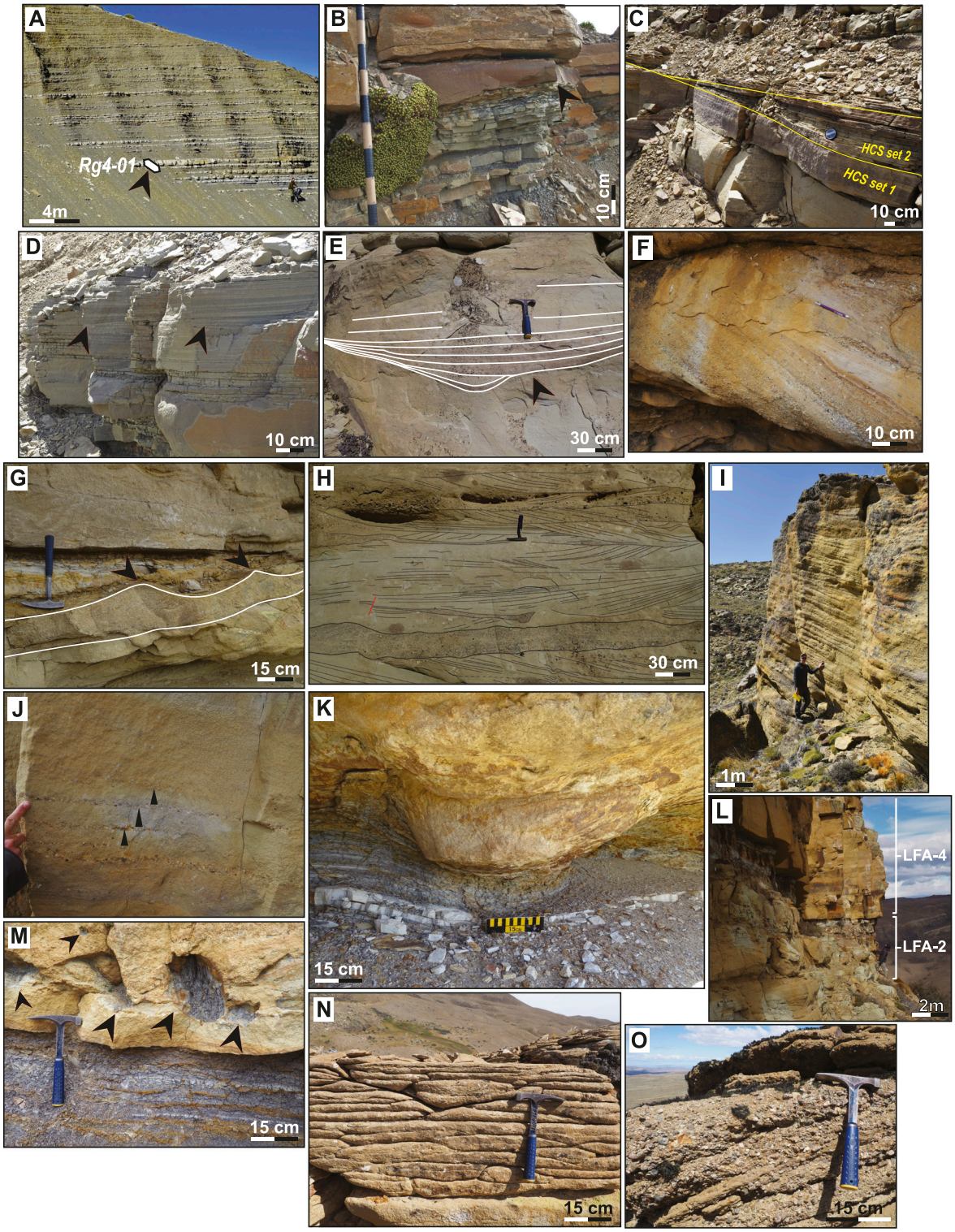

FIGURE 5 | Photographs of the La Anita Formation. **(A)** Outcrop scale example of the mud-rich portion of LFA-1 and location of sample RG4-01. **(B)** Bedset scale example of LFA-1 containing interstratified rippled fine-grained sandstone and mudstone units. Black arrow points to an erosive base of a fine-grained sandstone unit into finer grained units. **(C)** Example of Hummocky cross stratification sets from LFA-1. Yellow lines demarcate different HCS bedsets. Note the lateral thinning of HCS-1 into the background of the photograph. **(D)** Long wavelength, undulating beds of fine-grained sandstone beds from section SrC. Black arrows point to a gently dipping laminae set possibly indicative of deposition and reworking by storm-generated currents. **(E)** Example of fine-grained sandstone of LFA-2 with gently undulating, long wavelength scour fills composed of upward-flattening laminations. **(F)** Very coarse grained to pebble sized tabular cross bedded sandstone and conglomerate from

(*Continued*)

FIGURE 5 | LFA-3. **(G)** Very coarse grained to pebble sized rippled sandstone and conglomerate from LFA-3. White trace outlines the shape of the ripples; black arrows point to the ripple crests. Possible gravel oscillation ripples common in upper shoreface environments (cf. Clifton, 2006). **(H)** Example of most common outcrop exposure of LFA-3 containing multidirectional trough cross bedding with pebble-filled scours and current-ripple lamination. Black traces highlight bedsets and bed partings. Structureless 30 cm thick gravel unit defines the lower portion of the photograph. Red line highlights a small fracture offsetting strata. **(I)** Trough cross bed dune set composed of coarse sand and conglomerate deposited within a distributary channel from LFA-4. Axis of the channel points due south. **(J)** Fining upward sequences of beds from pebble conglomerate to medium-grained sandstone indicated by the black arrows common in LFA-4. **(K)** Load structure of medium to coarse-grained sandstone unit from LFA-4 into a recessive, mud-rich interval. Possible dinosaur trample marking. Scale is 15 cm across. **(L)** Sharp, likely erosional, contact between fine-grained LFA-2 sandstone and coarse-grained, channelized LFA-4 delta front sandstone. **(M)** Examples of mudstone rip up clasts common at the bases of channelized units from LFA-4. Black arrows point to mudstone rip-ups. **(N)** Relict planar laminated very coarse sandstone and pebble conglomerate from foreshore facies of LFA-5. **(O)** Weak unidirectional, tabular cross bedded pebble conglomerate from foreshore facies of LFA-5.

lithofacies and 5 lithofacies associations (**Table 1**). Lithofacies were selected based on bed/bedset lithologies, grain size, bedding geometries, sedimentary structures, and biotic assemblages (trace and body fossils). Recurring groupings of lithofacies were assigned a lithofacies association (LFA), which we define as a genetically related set of lithofacies representative of a distinct depositional environment (after Collinson, 1969; **Table 1**).

3.1 Lithofacies Association 1: Wave and Storm Influenced Lower Shoreface and Inner Shelf

Description. Thin-bedded heterolithic deposits of very fine to fine-grained sandstone and siltstone/mudstone with rare thicker-bedded hummocky cross-stratified sandstone compose lithofacies association 1 (LFA-1; Lithofacies 1–4; **Table 1**; **Figures 5A,B**). Towards the base of LFA-1, sandstone beds are fine-grained and thin-bedded with sharp and occasionally erosional bases into siltstone and mudstone beds (**Figure 5B**). Individual beds are <5 cm thick, whereas laminated heterolithic bedsets of interbedded sandstone and mudstone are on average ~30 cm thick. Beds are tabular and commonly continuous. However, some sandstone beds pinch and swell in thickness laterally. Bioturbation index (BI; Taylor and Goldring, 1993) is low (0–2) and LFA-1 contains a low diversity of trace fossil assemblages of vertical to sub-vertical burrows (*Ophiomorpha isp., Rhizocorallium isp.;* **Figures 6A,B**). Organic debris is common between sandstone laminae (**Figure 6C**). Current ripple to undulating/planar lamination in fine-grained sandstone beds are the most common sedimentary structures (**Figure 5B**). Hummocky cross-stratified (HCS), fine-grained sandstone beds are rare in mud-rich portions of LFA-1, although undulating to long wavelength cross-stratification is common (**Figures 5C,D**). In zones interpreted to be more proximal to fluvio-deltaic sources (see interpretation of LFA-4), hummocky and long wavelength cross bedding become the dominant sedimentary structure, sand to mud ratios increase, and beds appear to pinch and swell from several decimeters to a few centimeters in thickness in a laterally short (<5 m) distance.

Interpretation. We interpret LFA-1 to represent deposition onto the outer shelf and lower shoreface between storm and fair-weather wave base. Individual mudstone beds represent deposition via background sedimentation of fine-grained materials suspended in the water column via storms and currents. Hummocky cross-stratified, current rippled, and planar laminated beds likely formed from storm events via combined flows from oscillatory wave and unidirectional currents (Dumas et al., 2005; Dumas and Arnott, 2006; Plint, 2010). The common occurrence of interstratified mudstones suggests storm events were not powerful enough to erode and resuspend previously deposited sediment (Plint, 2010). The higher abundance of sands making up LFA-1 at section SrC (**Figure 4**) suggests increased proximity to fluvio-deltaic sources, which provided coarser sediment and higher amounts of organic detritus. Pronounced lateral variability in sandstone bed thicknesses at section SrC suggest these beds may be organized in shoreface sand ridges that trended oblique to the direction of shoaling (e.g., Snedden and Dalrymple, 1999).

3.2 Lithofacies Association 2: Wave and Storm Influenced Lower to Middle Shoreface

Description. Lithofacies association 2 (LFA-2) consists primarily of pervasively bioturbated, amalgamated white to gray, very fine to fine-grained sandstone (**Table 1**; Lithofacies 2, 4–5; BI = 4–6). The presence of interstratified mudstone beds reduces significantly compared to LFA-1. At outcrop scale, bed sets are tabular and laterally continuous. Individual beds commonly have gently undulating contacts with long wavelength (meter scale) scours filled with upward-flattening laminations (**Figure 5E**). Mud-lined sand-filled vertical to sub-vertical burrows (*Ophiomorpha isp.*; **Figure 6D**) are the only recognized trace fossils. Where bioturbation is less intense, relict sedimentary structures include undulating to planar laminations, swaley, very low-angle cross stratification, rare trough cross-bedding, coarse gravel lags defining the bases of beds, and rare soft-sediment deformation. Paleocurrent directions from cross beds are primarily southeast directed, with a lesser amount to the northeast (**Figure 4**). Isolated quartzite pebbles and cobbles are common. Plant debris and carbonaceous fragments are abundant throughout the lithofacies association.

Interpretation. LFA-2 represents deposition on the lower to middle shoreface of a wave-dominated, shallow-marine system. These sediments were deposited between storm and fair-weather wave bases, but at shallower depths than LFA-1 in which oscillatory energy from storm waves are powerful enough to erode muds deposited during fair weather conditions. Swaley cross-stratified, fine-grained sandstone beds that grade from heterolithic HCS are inferred to occupy the middle shoreface where aggradation rates and scouring potential is higher (Leckie and Walker, 1982; Dumas and Arnott, 2006; Plint 2010). The

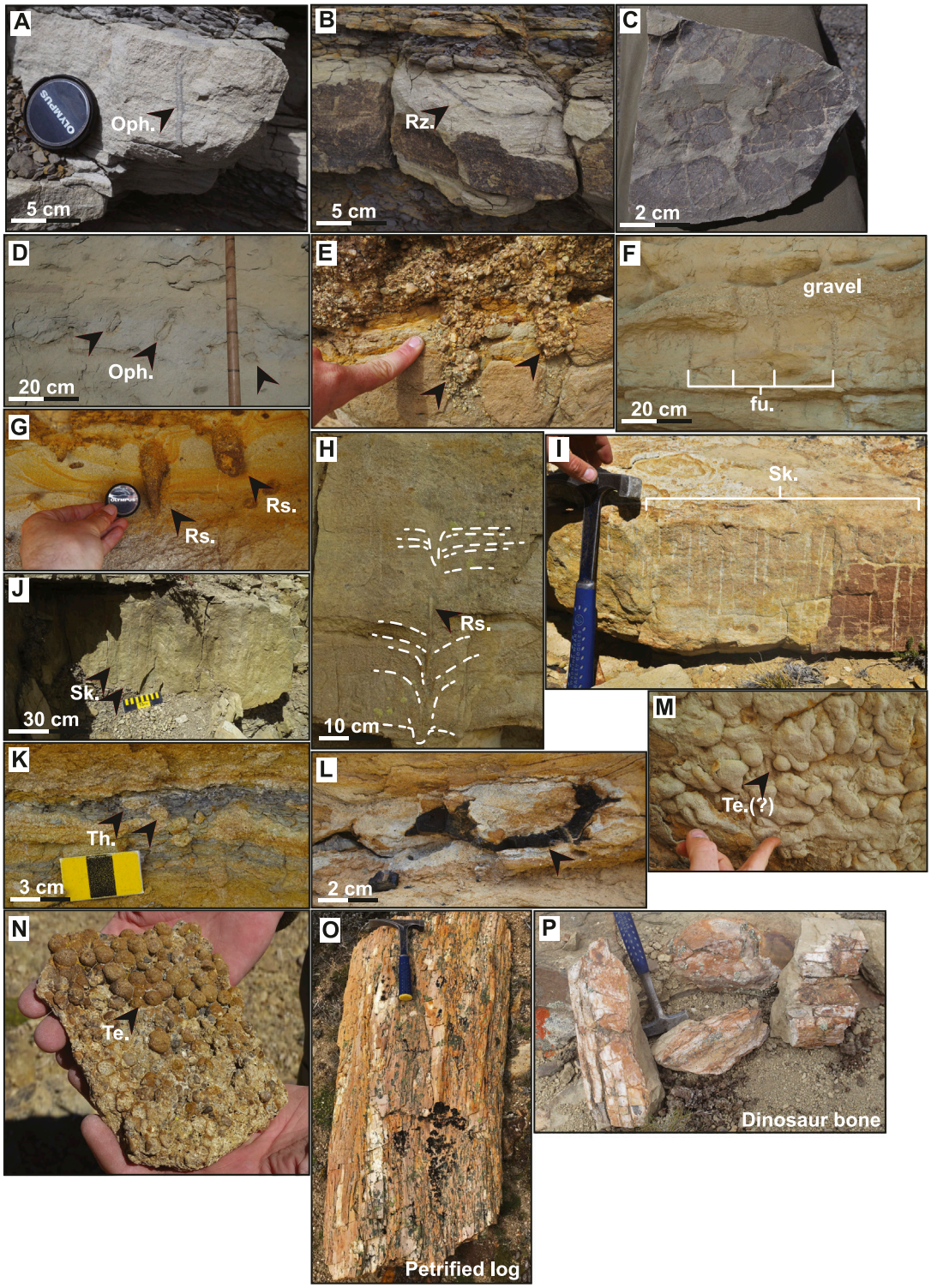

FIGURE 6 | Photographs of trace fossil and fossil assemblages from the La Anita Formation. **(A)** Sub-vertical, sand-filled, mud-lined *Ophiomorpha isp.*(Oph.) burrow from fine-grained sandstone of LFA-1. **(B)** Partially preserved sub-vertical to horizontal sand-filled burrow from LFA-1 of possible *Rhizocorallium isp.* (Rz.) affinity. **(C)** Organic plant debris on the base of a fine-grained sandstone bed commonly found defining laminated mud partings between sandstone beds in LFA-1. **(D)** Sub-vertical, mud-lined and sand-filled *Ophiomorpha isp.* burrow traces common in highly bioturbated portions of LFA-2. **(E)** Escape-equilibrium *fugichnia* trace fossils from LFA-3 outlined by pebble conglomerate infilling conical burrows in underlying sandstone unit. Black arrows point to escape structures. **(F)** Long (~30 cm in length) escape-equilibrium *fugichnia* trace fossils from LFA-3 at the base of a gravel unit into a coarse-grained sandstone. **(G–H)** Possible *Rosselia isp.* (Rs.) trace fossils from

(*Continued*)

FIGURE 6 | LFA-3. Dashed white traces in photograph H outlines contorted sandstone laminae by *Rosselia isp.* burrow. **(I–J)** *Skolithos isp.* (Sk.) ichnotaxa from LFA-4 sandstone units. **(K)** Possible horizontal *Thalassinoides isp.* (Th.) trace fossils into recessive organic mudstone interval from LFA-4. **(L)** Contorted coal bed from levee or interdistributary bar top facies from LFA-4. **(M)** Possible *Teredolites isp.* ichnotaxa defining the base of a sandstone bed into a recessive, organic rich mud interval from LFA-4. **(N)** *Teredolites isp.* ichnotaxa hand sample taken from LFA-4. **(O)** Large petrified log in float directly above outcrops of LFA-5. Logs of this size are common in the uppermost portions of LFA-5. **(P)** Fragments of a large dinosaur bone at the top of section RG-3 in LFA-5.

massive appearance of sand beds is attributed to the pervasive bioturbation throughout the unit. High BI values and overall burrowing uniformity throughout the section may suggest that physiochemical parameters for *Ophiomorpha isp.* burrowing biota were temporally stable and/or sedimentation rates were low enough to yield a low-stress environment for burrowers (MacEachern et al., 2010). Increased amounts of plant debris up-section and the presence of quartz pebbles and cobbles imply a proximity to fluvio-deltaic sources (Bhattacharya, 2010). We interpret stratigraphic sections with greater thicknesses of LFA-2 to reflect greater influence from wave energy (e.g., sec. RG-3; **Supplementary Figure S1**) whereas fluvio-deltaic influenced sections contain more distributary channel and mouth bar facies (e.g., secs. R40, CoC).

3.3 Lithofacies Association 3: High Energy Upper Shoreface

Description. Deposits of lithofacies association 3 (LFA-3) consist primarily of lower-medium to very coarse grained, cross bedded sandstone (Lithofacies 6–7) and subordinate amounts of thin-bedded rippled sandstone and siltstone (Lithofacies 1–2; **Figures 5F–H**). Average bed thickness is 48 cm and amalgamated bed sets reach several meters (~5 m) in thickness. Bed geometries consist of tabular bounding surfaces of inclined crossbed sets as well as erosive, trough-shaped, and laterally discontinuous surfaces infilled with cross-bedded conglomerate and sandstone. Organic-rich mudstone beds (<1 cm thick) occasionally mantle sandy bedforms. The most common sedimentary structure is multi-directional trough cross-bedding with pebble-filled scours and current-ripple lamination as well as rare gravel oscillation ripples (**Figure 5G**). Cross-stratified sandstone beds display moderate to poor sorting and outsized quartzite pebbles and cobbles are common. Paleocurrent directions from cross-stratified sandstone beds are diffusely to the south and southeast, with lesser amounts radially to the north (**Figure 4**; secs. SpC, CC, CgC). Sandstone beds are sporadically bioturbated (BI = 0–3) with *fugichnia* escape-equilibrium structures associated with *Rosselia isp.* and subordinate amounts of *Ophiomorpha isp.* and *Skolithos isp.* (**Figures 6E–H**).

Interpretation. LFA-3 represents the deposits of two- and three-dimensional dunes deposited on a high-energy, coarse-grained upper shoreface. These were deposited above fair-weather wave base where the influence of shoaling wave oscillatory flows, longshore drift, rip currents, and/or geostrophic flows facilitates the migration of subaqueous dunes resulting in multi-directional trough and tabular cross-bedding (Clifton, 2006; Plint, 2010). The availability of coarse-grained sandstone and pebble conglomerate suggests proximity to fluvio-deltaic sources. Poor sorting, outsized clasts, *fugichnia* escape structures, and the decrease in bioturbation index and burrowing uniformity suggest that sedimentation rates were high (Clifton, 2006; MacEachern et al., 2010; Plint, 2010). Rare organic-rich mudstone drapes suggest intermittent periods of quiescence between storm-induced dune migration events (Plint, 2010).

3.4 Lithofacies Association 4: Fluvial-Influenced Delta Plain Interdistributary Channels and Bars

Description. Medium-lower to very coarse-grained, occasionally amalgamated sandstone and moderately to poorly sorted pebble conglomerate primarily make up lithofacies association 4 (LFA-4; Lithofacies 6–10, **Figure 5I–M**; **Table 1**). Subordinate amounts of fine-grained, planar to current-ripple laminated sandstone, siltstone, and carbonaceous mudstone also are present (Lithofacies 1–2; **Table 1**). Sandstone thicknesses range from 10 to 120 cm (avg. thickness = 31 cm) with cross-bedded or massive bed sets bounded by recessive intervals or erosional surfaces reaching up to ~3–4 m in relief (**Figure 7**). Both tabular and erosive geometries are present at outcrop scale. Several bounding surfaces have channel-like geometries which scour and erode adjacent beds up to ~2 m (**Figure 7**). The predominant sedimentary structure is dune-scale trough and planar, unidirectional crossbedding. Bases of crossbeds commonly contain gravel lags and mudstone rip-up clasts (**Figure 5M**). Paleocurrent directions from crossbeds are radially southward directed (**Figure 4**; secs. R40 and CoC). Current-ripple lamination, planar lamination, and graded beds are also present (**Figures 5I,J**). Large-scale (~1–2 m) load structures are present at the bases of thick amalgamated sandstone units into recessive heterolithic deposits (**Figure 5K**). Finer-grained heterolithic intervals commonly contain interstratified carbonaceous mudstone that drape fine-grained current-ripple laminations. At the base of section CoC, LFA-4 sandstone beds are in sharp, likely erosional contact with fine-grained, moderately bioturbated sandstone of LFA-2 affinity (**Figure 5L**). Bioturbation throughout the section is low (BI = 0–2) and decreases upsection. Burrowing intensity is non-uniform between beds. *Fugichnia* escape structures, *Rosselia isp.*, *Ophiomorpha isp.,* and *Skolithos isp.* ichnotaxa are present in the sandstone beds (**Figures 6I,J**). Ichnotaxa within carbonaceous, heterolithic fine-grained sandstones and mudstones include *Ophiomorpha isp., Thalassinoides isp.*, *Teredolites isp.,* and possible *Arenicolites* ichnospecies (**Figures 6K–N**).

Interpretation. Facies assemblages and ichnofacies of LFA-4 are consistent with a river-dominated, coarse-grained delta-front environment reflecting high-rates of deposition from decelerating unidirectional flows within distributary channels and adjacent mouth bars. The coarse grain size, sedimentary structures, and paucity of fine-grained units suggest constant reworking of

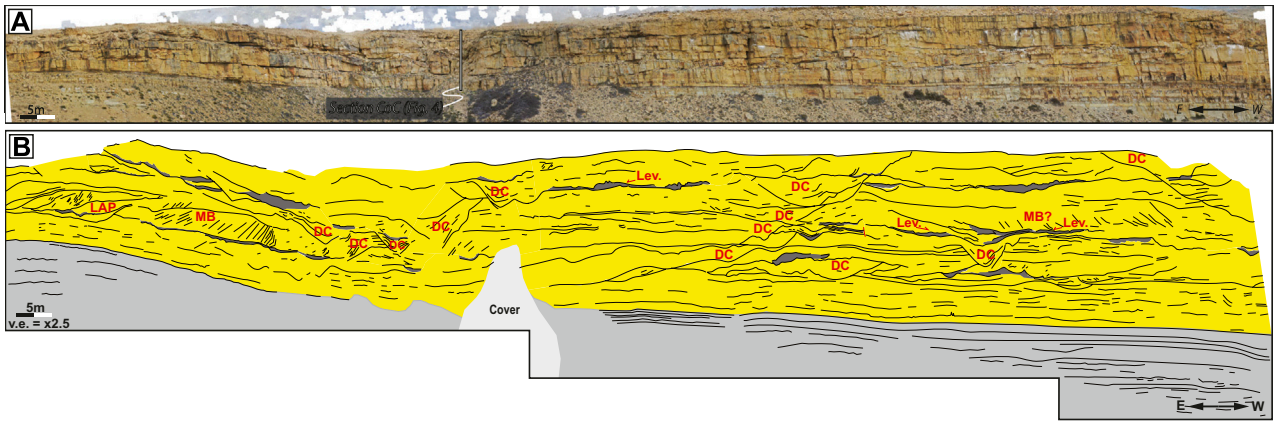

FIGURE 7 | (A) Photo-orthomosaic of a La Anita Formation cliff face where section CoC was measured. **(B)** Vertically exaggerated (x2.5) interpretation of above photo-orthomosaic with labeled distributary channels (DC), mouth bars (MB), levees (lev.), and lateral accretion packages (LAP). Yellow units are sandstone dominant, gray units are recessive and mudstone dominant.

sediments by tractive currents. Sedimentation rates were high as evidenced by graded beds, variable poor sorting, load structures, and high abundance of *fugichnia* escape structures (Bhattacharya, 2010). Large 1–2 m thick load structures at the base of sandstone beds may be dinosaur track imprints (**Figure 5K**), which is consistent with the large amount of fossilized dinosaur bones throughout terrestrial units of the Austral sector of the basin (e.g., Novas et al., 2008; Lacovara et al., 2014). The majority of the distributary channels are infilled with massive sandstone beds interpreted as infill from migrating mouth bars. Other channels display lateral accretion packages, suggesting these channels were long-lived enough to migrate laterally over time (**Figure 7**). Trace fossil assemblages attributed to the *Skolithos* ichnofacies assemblage suggest an open to brackish marine environment with high levels of wave/current energy within clean, noncohesive substrates (MacEachern et al., 2010). The erosive, channel-like, and tabular cross-stratified bed set geometries are consistent with a mouth bar succession separated by terminal distributary channels (Olariu and Bhattacharya, 2006; Bhattacharya, 2010). Fine-grained, recessive heterolithic units with abundant plant debris and higher rates of bioturbation likely reflect mouth bar tops and/or levees of adjacent channels (**Figure 7**). Abundant plant debris, gravel deposits, and mud rip-up clasts common at bases of channels suggest a strong fluvial influence on large-scale delta morphology.

3.5 Lithofacies Association 5: Gravel-Rich Foreshore

Description. The uppermost exposed strata from the La Anita Formation in the Zona Centro region (**Figure 3A**) consist of fine to coarse-upper sandstone to pebble conglomerate with well-segregated, pancake-shaped lenses of massive gravel interbedded with undulating laminated and cross-bedded sandstone (LFA-5; Lithofacies 11–12; **Figures 5N–O**). Bed thicknesses are approximately 10 cm and beds are tabular, albeit undulating, at outcrop scale. Large (up to 1.5 m in length) fragments of petrified wood, dinosaur bones (**Figures 6O–P**), and root structures are commonly associated with this unit. A recessive, poorly exposed mud-rich, interval overlies this unit and forms a mesa with abundant large (decimeter to meter scale) pieces of petrified wood in float.

Interpretation. LFA-5 represents deposits of a gravel-rich nearshore environment. While individual planar laminations are difficult to identify, the well-segregated, pancake-shaped bedding style may be relict laminations found in a foreshore swash zone or the uppermost shoreface environment (Clifton, 2006). The presence of large dinosaur bones, transported logs of petrified wood, and root structures suggest LFA-5 was deposited in a marginal-marine to terrestrial environment. Well-segregated layers of gravel beds may be indicative of grain size and density partitioning produced by wave swash on the foreshore (Clifton, 1969; Clifton, 2006). The poorly outcropping, muddy interval above LFA-5 is consistent with a low-energy environment such as backshore deposits of a coastal plain. Pervasive cover of this unit, however, prevents further investigation.

3.6 Paleocurrent Measurements

We present 193 new paleocurrent measurements sampled from trough and planar cross bedded sandstone and gravel conglomerate from the La Anita Formation. Rose diagrams of paleoflow directions are plotted according to which stratigraphic section the measurements were taken from (**Figure 4**). In general, our results demonstrate that the paleoflow direction was radially to the south and southeast. These results are consistent with the findings from other workers (Moyano Paz et al., 2018; Sickmann et al., 2019). Paleocurrent directions from sections with interpreted fluvio-deltaic influence (secs. R40, CoC, SpC) record radial dispersion of paleoflow broadly to the south while those from open shoreface and foreshore environments

(secs. CC, FC, CgC, RG-3) record a southeast flow direction with subordinate paleoflow to the northeast.

3.7 Depositional Environment of the La Anita Formation

We interpret the La Anita Formation to be deposited in a fluvially dominated and wave- influenced delta and storm and wave-influenced shoreface. The succession records a progradational shelf with basal offshore to lower shoreface facies (LFA-1) overlying continental slope facies of the Alta Vista Formation, which transitions into shoreface and laterally variable foreshore or delta-front environments. An increase in sediment grain size, terrestrial and marginal marine facies and sedimentary structures (e.g., coal beds, rooted horizons, distributary channels, dune-scale cross bedding), and a decrease in heterolithic interstratified mudstone beds and storm-induced event beds are consistent with a prograding delta environment. East-to-west lateral variability from gravelly delta-front mouth bars and channel complexes to wave and storm-influenced upper shoreface and foreshore deposits suggests a lateral transition in depositional environments across the upper La Anita Formation. Thus, sections of the La Anita Formation in the eastern portion of the study area (secs. CoC, R40, SrC, SpC(?)) were in closer proximity to, and likely a part of, the fluvio-deltaic point source providing the majority of the coarse-grained fraction into the basin. Whereas sections further west (e.g., secs. CC, FC, CGC, RG-3) were likely deposited on an open shoreface in which wave and current energy reworked sediments. Channelized beds, lateral accretion packages, coarse sediment size, pebble-sized conglomerate, poor sorting, large petrified logs, and carbonaceous levee deposits all suggest strong fluvial influence on the deltaic portions of the formation. Sedimentation rates were likely consistently high given the pervasive amount of *fugichnia* escape trace fossils and load structures present in the sandy portions of the unit.

The abrupt contact between fine-grained, pervasively bioturbated sandstone with massive, channelized medium–coarse grained sandstone may represent the contact between the prograding delta front and prodelta (**Figure 5L**). Paleocurrents are generally to the east-southeast and southeast. Longshore drift and currents generated on the western shoreface may have translated sediment laterally to its deltaic counterparts, producing a mixed river and wave influenced, asymmetric delta system. The ichnofacies present are broadly consistent with a shoaling shallow-marine to marginal marine environment in a moderately physiochemically stressed environment due to high rates of sedimentation (MacEachern et al., 2010; Moyano Paz et al., 2020). Facies analysis by Moyano Paz et al. (2018) proposed that the La Anita Formation should be divided into two informal units bounded by a regional surface of erosion marked by a prominent (ca. 5 m thick) coal bed. From this, those authors argued that the La Anita Formation is composed of two genetically unrelated deltas—with a lower, wave-influenced unit and upper fluvial-influenced unit—driven by a sea-level regression. Stratigraphic sections from this study did not identify any evidence that suggests more than a single prograding facies succession making up the La Anita Formation. Maximum depositional age data from these sections also support coeval deposition of these strata (see **Section 4.4**). We therefore interpret the La Anita Formation as one progradational unit with lateral facies variability producing mixed input from river and wave activity across an asymmetric delta system. Sections from this study are north of most of the sections reported by Moyano Paz et al. (2018), which may only capture the wave-dominated, fluvial-influenced deltaic lower interval described by those authors.

4 DETRITAL ZIRCON AND ASH GEOCHRONOLOGY

4.1 Sampling Strategy and Analytical Methods

A total of 20 sandstone samples were collected from the Upper Cretaceous Alta Vista (N = 4; n = 1,159) and La Anita Formations (N = 16; n = 4,060) for U-Pb detrital zircon analysis (Table 2; **Supplementary Table S1**; **Figure 8**). We also present five new zircon U-Pb ages of volcanic ashes from a ca. 250 m thick section of the Alta Vista Formation consisting of interbedded fine-grained sandstone and mudstone (sec. AV-1; **Figure 3A**; **Table 2**; **Supplementary Table S1**). Fine to medium-grained, well sorted sandstones were sampled to minimize the potential effects of grain size bias on provenance signatures. Sandstone and ash samples were crushed and zircons were isolated using common mineral separation techniques including a Gemini water table, magnetic separation, and heavy-liquid separation procedures (e.g., Gehrels, 2000; Fedo et al., 2003; Gehrels et al., 2008) at Stanford University's Earth Materials Preparation Lab. Measurements of U-Th-Pb isotopic ratios from detrital zircon were made using laser ablation-inductively coupled plasma-mass spectrometry (LA-ICP-MS) with either a Nu or Element 2 mass spectrometer at the University of Arizona LaserChron Center following standard analytical methods (e.g., Gehrels et al., 2008; Gehrels and Pecha, 2014). Individual zircons were ablated using Photon Machines Analyte G2 excimer lasers that delivered a 30 μm beam to hand-selected crystal locations. To prevent biasing of differential grain size, zircon spots were selected by choosing grains that were the minimum distance to a spot along an evenly spaced grid of spot locations. Standardized zircon reference material SL-2 (563 Ma; Gehrels et al., 2008) was used to calibrate analyses between every 5 unknown analyses. The Plešovice zircon (337.71 ± 0.37 Ma; Sláma et al., 2008) was used as a secondary standard to assess machine drift at the beginning and end of each run. Approximately 300 grains were targeted per sample. U-Th-Pb ratios that had >10–15% precision, >30% discordance, >5% reverse discordance or >200–400 Pb counts per second were excluded from age interpretation. Due to precision cutoffs in isotopic chronometers, all reported ages <1 Ga are $^{206}Pb/^{238}U$ measurements while >1 Ga grains are $^{206}Pb/^{207}Pb$ ratios with 1σ errors. Data were reduced at the Arizona LaserChron Center using Iolite v. 2.31 software in WaveMetrics Igor Pro following Gehrels et al. (2008) and Gehrels and Pecha (2014).

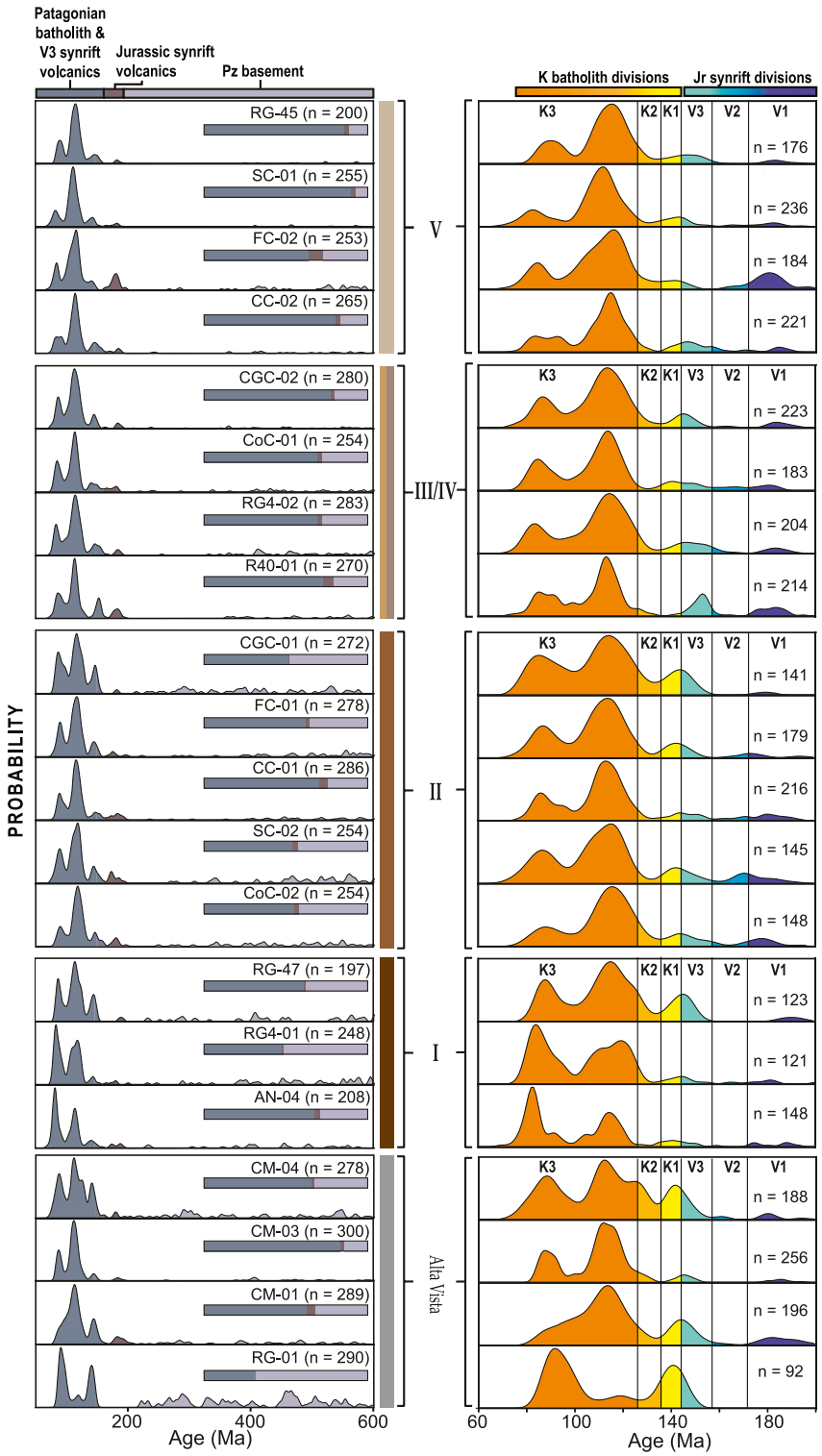

FIGURE 8 | Kernel density estimates (bandwidth = 5) and age distribution bar charts of detrital zircon results from the Alta Vista and La Anita Formations from 60 to 600 Ma (left column) and 60–200 Ma (right column). 60–600 Ma age data are separated into Patagonia volcanic arc, Early Jurassic massif units, and Paleozoic basement materials. 60–200 Ma age data are divided by periods of Cretaceous Patagonian arc magmatism (144–137 Ma (K1), 136–127 Ma (K2), and 126–75 Ma (K3); Hervé et al., 2007) and Jurassic silicic volcanic events (188–178 Ma (V1), 172–162 Ma (V2), and 157–142 Ma (V3); e.g., Pankhurst et al., 2000) La Anita Formation samples are grouped according to interpreted lithofacies association (labeled in the center colored rectangles and roman numerals).

TABLE 2 | List of maximum depositional ages and ash ages from the Alta Vista and La Anita Formations.

TABLE 2A La Anita Formation maximum depositional age calculations

Section	Sample	YSG	Uncertainty	YC1σ(2+)	Uncertainty	YC2σ(3+)	Uncertainty	Type	Location (°)	
									Latitude	Longitude
R40	R40-02	73.3	0.38	82	0.32	83.1	0.15	DZ	−49.9038	−72.061
SrC	Rg4-01	74.4	0.3	80.6	0.36	79.9	0.36	DZ	−49.8974	−72.4043
CoC	CoC-02	79.7	2.1	81.3	1.12	83.6	0.69	DZ	−49.907	−72.405
CoC	CoC-01	78.5	1.81	79.3	1.36	82.3	0.39	DZ	−49.9071	−72.4038
SpC	SpC-02	74.5	3.3	77.6	1.48	79.5	0.93	DZ	−49.9203	−72.4172
SpC	SpcC-01	68.5	3.99	73	1.72	75.3	1.29	DZ	−49.9206	−72.4166
ChC	ChC-01	78.2	2.57	78.3	1.93	82.3	0.58	DZ	−49.9226	−72.422
ChC	ChC-02	75.2	4.47	80.1	1	82.6	0.47	DZ	−49.9231	−72.4219
FC	FC-01	77.1	2.32	78.7	1.43	84.8	0.33	DZ	−49.9176	−72.4335
FC	FC-02	70.5	5.9	77.3	1.87	81.2	0.8	DZ	−49.9178	-−72.4336
CgC	CgC-01	78.7	0.89	79.1	0.65	80.2	0.51	DZ	−49.9041	−72.4558
CgC	CgC-02	75.7	4.92	79	1.04	82.7	0.63	DZ	−49.9052	−72.4561
RG-3	RG-47	83.9	0.98	85.2	0.32	85.4	0.29	DZ	−49.9075	−72.4652
RG-3	RG-45	84.2	0.88	84.8	0.37	85.9	0.25	DZ	−49.9062	−72.4661

TABLE 2B Alta Vista Formation maximum depositional age calculations and ash age calculations

Section	Sample	YSG	Uncertainty	YC1σ(2+)	Uncertainty	YC2σ(3+)	Uncertainty	YSP[a]	Uncertainty	Type	Location (°)	
											Latitude	Longitude
AV-1	AV1-01	87.9	1.26	89.5	0.57	90.6	0.39	90.43	0.51	Ash	−49.925	−72.5597
AV-1	AV1-03	85.3	0.99	86.4	0.49	87.6	0.3	86.3	0.5	Ash	−49.9239	−72.5553
AV-1	RG-02	85.8	0.79	86.4	0.5	87.5	0.33	87.33	0.33	Ash	−49.9239	−72.5553
AV-1	AV1-04	85	1.06	86.2	0.4	87.5	0.23	87.68	0.22	Ash	−49.9241	−72.555
AV-1	AV1-06	85.1	0.66	85.5	0.34	86.5	0.19	86.4	0.2	Ash	−49.9242	−72.5537
AV-1	RG-01	85	1.54	86.7	0.54	88.2	0.26			DZ	−49.9239	−72.5553
CM	CM-01	84.2	0.77	84.8	0.4	85.1	0.39			DZ	−49.9547	−72.7113
CM	CM-03	84.7	0.68	85.3	0.24	86	0.19			DZ	−49.9555	−72.7088
CM	CM-04	72.9	0.39	77.1	0.36	79	0.19			DZ	−49.9575	−72.7041

[a]*YSP, calculated for ash ages only.*

4.2 Data Visualization and Multidimensional Scaling

Kernel density estimates and cumulative frequency diagrams of detrital zircon data, weighted mean averages for depositional age analysis, and multidimensional scaling plots were created using both the detritalPy Python module (Sharman et al., 2018) and DZStats/DZ MDS softwares (Saylor and Sundell, 2016). Individual kernel density estimate plots (bandwidth = 5) were plotted for each individual sample (**Figure 8**). Plots were colored according to known source locations with distinguishable age ranges, which are also represented as bar graphs for each sample (**Figure 8**). Samples from the La Anita and Alta Vista Formations were subgrouped by interpreted lithofacies associations (see **Section 3**) in order to assess the relationship between lithofacies and provenance signatures (**Section 5.1**).

Calculations of maximum depositional ages (MDA) are reported in **Table 2**. We present results from the youngest single grain (YSG) per sample, and weighted mean averages from both the youngest 2+ grains within 1σ uncertainty (YC1σ(2+)) and the youngest 3+ grains within 2σ uncertainty (YC2σ(3+); Dickinson and Gehrels, 2009). We opt to use the more conservative YC2σ(3+) MDA method as estimates for depositional ages to avoid estimates that may be younger than the true depositional age (cf. Coutts et al., 2019; Sharman and Malkowski, 2020). Depositional age calculations for ashes were determined using the Youngest Statistical Population (YSP) method (i.e., Coutts et al., 2019; **Table 2**). This method calculates a maximum depositional age as a weighted average of the subset of ≥2 zircon grains that yield a mean square weighted deviation (MSWD) of approximately 1. We utilize multidimensional scaling (MDS) plots (e.g., Vermeesch, 2013; Vermeesch, 2018) to assess multi-sample detrital zircon age spectra dissimilarities across all samples from the La Anita and Alta Vista Formations. These plots represent a "map" onto a dimensionless plane or space wherein samples that are more similar to each other—according to the comparative metrics—plot closer to each other. Conversely, dissimilar samples plot further away from each other. This transformation is achieved through an iterative process that attempts to minimize the misfit, also known as the "stress" value, between degree of correspondence of MDS map distances and the comparative matrix selected by the user. High stress values (>0.1; Kruskal, 1964) indicate a poor fit wherein the dimensional "flattening" of data onto a plane or space yields distortions unrepresentative of the actual comparative metrics. We use both the V value of the Kuiper test and the D value of the Kolmogorov-Smirnov (K-S) test, as well as a metric-squared stress criterion for transforming matrices onto an MDS plane while maintaining the lowest possible stress values. Resulting V and D value MDS plots yield stress values of 0.14 and 0.08 respectively (**Supplementary Figure S2**). These

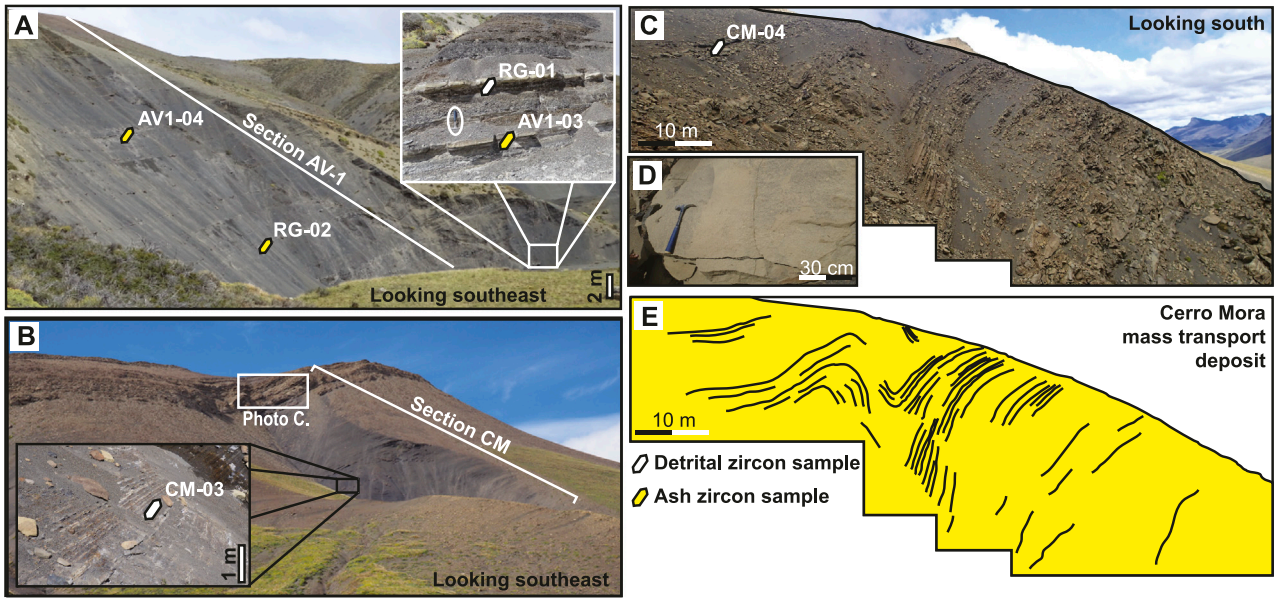

FIGURE 9 | Photographs from described Alta Vista Formation sections. **(A)** Outcrop scale photograph of section AV-1. Note the predominance of gray thin-bedded mudstone making up this section. Inset image provides an enhanced view of the strata as well as sample locations for samples AV1-03 and RG-01. **(B)** Photograph of Cerro Mora (**Figure 3A**). Note the thick bedded, buff colored sandstone beds capping the section. Inset image shows an example of strata lower in section CM, which still contains abundant thin-bedded sandstone units. **(C)** Outcrop scale photograph of the top portion of section CM. Note the abundance of thick-bedded, amalgamated sandstone beds. **(D)** Example of a typical sandstone bed that makes the upper portion of section CM. These sandstone units are massive, fine-grained, and occasionally contain water-escape features reminiscent of high-density turbidite deposits (cf. Lowe, 1982). **(E)** Trace drawing interpretation of contorted and folded stratigraphy in photograph **(C)**. Note the isoclinal anticline and syncline pair defining the summit of Cerro Mora. We interpret this large fold to be a part of a mass transport deposit associated with submarine landsliding.

reasonable stress values indicate that distances represented on these maps are reliable for multi-sample dissimilarity comparisons across the Alta Vista and La Anita Formations.

4.3 Age of the Alta Vista Formation

Interstratified tuffaceous rocks from a 250 m thick section (section AV-1; **Figure 3A**; **Figure 9A**) of mudstone and thin-bedded turbidites were sampled from outcrops of the Alta Vista Formation approximately 3 km west of the primary study location in Zona Centro (**Figure 3A**). We present calculated weighted mean ages using the Youngest Statistical Population method (see **Section 4.2**) of these ash beds as well as a detrital zircon maximum depositional age from one interstratified fine-grained sandstone from this section (sample RG-01). We also calculate maximum depositional ages from three samples collected from ca. 600 m thick exposure of the Alta Vista Formation near Cerro Mora (sec. CM; **Figure 3A**). Zircon U-Pb ages from ash beds range from 90.43 to 86.30 Ma while detrital zircon maximum depositional ages are between 88.2 and 79 Ma (**Table 2**). Ash bed ages bracket the depositional age of the Alta Vista Formation between the late Turonian and early Santonian while a maximum depositional age from the uppermost exposed portion of the Alta Vista Formation extends its potential maximum age to the middle Campanian (**Figure 3B**).

Previous studies bracketed the depositional age of the Alta Vista Formation between the late Santonian and middle Campanian (Macellari et al., 1989; Arbe, 2002; Sickmann et al., 2018). Based on these new ash age results, we suggest that deposition of the lower Alta Vista Formation onto the continental slope may have been active as early as the late Turonian. Basin shoaling and coeval deposition of shallow-marine deposits of the La Anita Formation occurred by ca. 86 Ma based on contemporaneous Alta Vista ash ages and the maximum depositional ages from the La Anita Formation from both this study and others (Sickmann et al., 2018; Ghiglione et al., 2021; **Table 2**).

4.3.1 Aggradation Rates of the Alta Vista Formation

A linear regression of ash age data versus section height from the Alta Vista Formation yields a mean aggradation rate for the lower Alta Vista Formation of 34 m Myr^{-1} (R^2 = 0.72). This value falls within the lower range of shelf-margin aggradation rates observed from both modern and ancient continental margins (e.g., Carvajal et al., 2009), and is significantly lower than the Campanian–Maastrichtian Tres Pasos-Dorotea delta-slope system from the Magallanes portion of the basin (Tres Pasos Formation: 252–800 m Myr^{-1}, Daniels et al., 2018; Dorotea Formation: 189.9 m Myr^{-1}, Schwartz et al., 2017). The lower sedimentation rates calculated from the Alta Vista Formation suggest that—at least prior to the deposition of the fluvio-deltaic and shallow-marine sequences of the La Anita Formation—this portion of the continental slope did not receive high amounts of sediment. Instead, this region of the slope was dominated by

mud-rich deposits and thin-bedded turbidites derived from distal turbidity currents. Re-entrainment and transport of material into the basin was facilitated by debris flows in this region (**Figure 9A**). Evidence of mass-transport deposits from debris flow events are common throughout the Alta Vista Formation, where in some cases tens of meters-thick stratigraphic sections have been folded and overturned via submarine landsliding (**Figures 9B–E**).

4.4 Age of the La Anita Formation

Calculated MDAs from the La Anita Formation range from 85.9 to 75.3 Ma, with all but one sample bracketed between ca. 86–80 Ma (**Table 2**). This places the age of the La Anita Formation between late Santonian and early Campanian, which is consistent with MDA estimates presented in previous studies (Sickmann et al., 2018; Ghiglione et al., 2021). These results are also in partial agreement with Campanian assignments of ammonite fossils from the lower La Anita Formation (Arbe and Hechem, 1984; Macellari et al., 1989; Kraemer and Riccardi, 1997; Arbe, 2002). We argue that the MDAs are, in general, apt approximations of a true depositional age due to 1) the broad agreement between these age data and biostratigraphic constraints, 2) the proximity of the active Andean arc (Hervé et al., 2007), which provided the ca. 60% of all analyzed zircons from this study, and 3) consistency with results presented from other Cretaceous formations in the Magallanes-Austral Basin (e.g., Bernhardt et al., 2012; Malkowski et al., 2017a; Malkowski et al., 2017b; Schwartz et al., 2017; Daniels et al., 2018; Malkowski et al., 2018) that have demonstrated age agreement between calculated MDAs and other geochronological methods such as biostratigraphic data and volcanic ash U-Pb geochronology.

Maximum depositional ages across measured sections are commonly in the same age ranges within uncertainty. An exception to this observation is from section SpC, which yielded two younger, middle Campanian MDAs (79.5 ± 0.93 Ma and 75.3 ± 1.29 Ma; **Table 2**). While this section is along-strike from adjacent measured sections across the study area, section SpC is located near the axis of a shallowly dipping (<5° dipping limbs) syncline (Ghiglione et al., 2014). This structural low may have produced a zone of increased stratigraphic preservation in the region, which could have sheltered younger strata within a zone of reduced uplift and erosion.

4.5 Age Correlation Between Austral and Magallanes Basin Sectors

Using ash ages and detrital zircon MDAs from the Alta Vista and La Anita Formations, we compare the stratal ages from the Austral (Argentine) portion of the basin to those in the Magallanes (Chilean) portion of the basin using a recently updated chronostratigraphy compiled by Daniels et al. (2019) (**Figure 3B**). New age data presented herein provide the most detailed chronostratigraphic constraints of the Alta Vista and La Anita Formations, which places their depositional timing between 90.43–79 Ma and 85.9–75.3 Ma, respectively. These age ranges have the most overlap with the abyssal plain facies and deep-water coarse clastic sediments of the Cerro Toro Formation (ca. 90–80 Ma; Daniels et al., 2019; **Figure 3B**). The Alta Vista Formation coincides mostly with the lower siltstone prone member of the Cerro Toro Formation (ca. 90–86 Ma) whereas the La Anita Formation has the most overlap with the Lago Sofia conglomerate defining the upper portion of the Cerro Toro Formation (ca. 88–81 Ma). One sample from the Alta Vista Formation produced an MDA (sample CM-04 YC2σ(3+) MDA = 79.0 ± 0.19 Ma; **Table 2**) that comports with the earliest slope mass transport deposits of the lower Tres Pasos Formation (80.5–77.4 Ma). One sample from the La Anita Formation produced an MDA (sample SpC-02 YC2σ(3+) MDA = 75.3 ± 1.29 Ma; **Table 2**) that overlaps with the shelf-slope clinoform deposits of the upper Tres Pasos and Dorotea Formations (77.4–67.1 Ma). This may suggest that the progradation of these units continued into the late Campanian. However, given that all but two samples coincide with the timing of the Cerro Toro Formation deposits, we argue that the Cerro Toro Formation is the most likely candidate as a genetically related southern counterpart to the Turonian through middle Campanian deposits of the northern depocenter. Further sampling of the uppermost Alta Vista and La Anita Formations is necessary to better constrain the latest depositional ages for these units. The co-appearance of deep-water conglomeratic facies from the upper Cerro Toro Formation with coarse-grained, shallow-marine deposits of the La Anita Formation may signal a synorogenic sedimentation event controlled by the progressive easterly advance of the orogenic front in the Austral and Magallanes portions of the basin (Ghiglione et al., 2021). Late Coniacian through early Santonian progradation of the Austral continental slope occurred in concert with the deposition of the deep-water Lago Sofia conglomerate, although deposition of lower Alta Vista Formation (sometimes grouped with the Cerro Toro Formation; e.g., Ghiglione et al., 2014; Sickmann et al., 2018; Sickmann et al., 2019) occurred as early as the late Turonian (ca. 90 Ma).

4.6 Potential Source Terranes

Three primary detrital components make up the provenance spectrum recorded in siliciclastic units of the Magallanes-Austral Basin: 1) pre-Jurassic metamorphic complexes representing uplift of basement rock via fold-and-thrust belt deformation to the west (>200 Ma), 2) Jurassic volcanic and volcaniclastic rocks associated with synrift volcanism as a result of the breakup of Gondwana (ca. 188–142 Ma), and 3) latest Jurassic and Cretaceous volcanic and magmatic materials derived from the Patagonian arc and batholith (ca. 157–75 Ma). These sectors can be delineated by their unique assemblage of geochronological ages in magmatic and recycled zircons from both primary and recycled sources. The following sections provide detail for each source area.

4.6.1 Pre-Jurassic Metamorphic Basement

A series of Devonian–Triassic metamorphic basement terranes within the fold-and-thrust belt at the ~74°W meridian provided Precambrian through Triassic recycled zircon to the basin (**Figure 10**; Faúndez et al., 2002; Hervé et al., 2003; Hervé

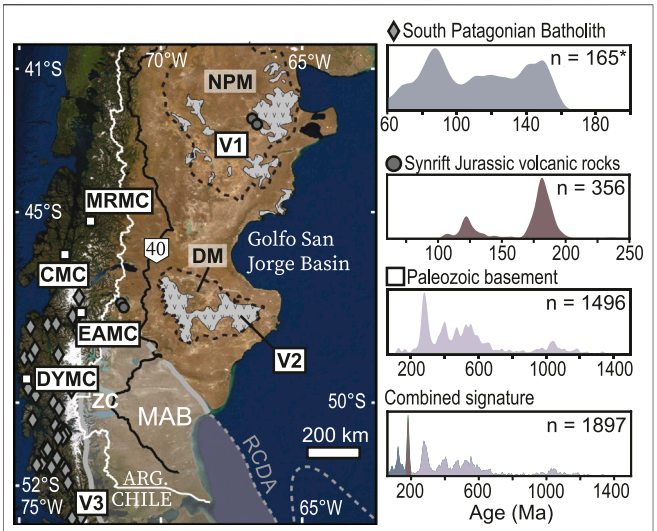

FIGURE 10 | Map of southern South America with traces of the Magallanes Austral basin (MAB) and proposed source locations. Individual markers correspond to sample locations compiled from other workers from Paleozoic metamorphic basement terranes (Herve et al., 2003; Hervé and Fanning, 2001; Herve et al., 2010), distal Jurassic terranes (Ghiglione et al., 2015; Navarro et al., 2015) and the South Patagonian Batholith (Herve et al., 2007). Resulting compilations are plotted as kernel density estimate plots both individually and as a combined signature. Zones of Jurassic silicic volcanic events are labeled as V1 (188–178 Ma), V2 (172–162 Ma), and V3 (157–142 Ma) (e.g., Pankhurst et al., 2000). NPM, North Patagonian Massif; DM, Deseado Massif; ZC, Zona Centro; ARG, Argentina border; RCDA, Rio Chico Dungeness Arch; MRMC, Main Range metamorphic complex; CMC, Chonos metamorphic complex; EAMC, Eastern Andean metamorphic complex; DYMC, Duque de York metamorphic complex. Not shown but a part of the analysis: Cordillera Darwin metamorphic complex (~54°S, 70°W). *N values for the Patagonian batholith are weighted average results from the analysis of several granitic zircons per sample.

et al., 2008; Hervé et al., 2010; Calderón et al., 2016; Suárez et al., 2019). Paleozoic meta-igneous and metasedimentary units also underlie the North Patagonian and Deseado Massifs to the northeast (**Figure 10**; Pankhurst et al., 2006; Chernicoff et al., 2013; Moreira et al., 2013). Detrital zircon spectra from these basement units display a prominent Permo-Triassic age peak (310–260 Ma; **Figure 10**) as well as secondary amounts of Proterozoic (1,200–900 Ma), Cambro–Ordovician (550–450 Ma), and Devonian–Early Mississippian (410–350 Ma) grains. Minor components of grains >1,200 Ma make up ~3–10% within each metamorphic complex.

4.6.2 Synrift Jurassic Volcanic Rocks

Jurassic silicic volcanic events associated with the breakup of Gondwana produced the Chon Aike large igneous province in eastern Patagonia and the Andean Cordillera (Gust et al., 1985; Pankhurst et al., 1998; Pankhurst et al., 2000). Ages of associated volcanic rocks range from ca. 190–150 Ma and are divided by three major pulses of volcanic activity across the region: V1 (188–178 Ma), V2 (172–162 Ma), and V3 (157–142 Ma) (**Figures 8**, **10**; Pankhurst et al., 2000; Calderón et al., 2007). Associated magmatic pulses are geographically divided and represent a southwestward migration of diachronous extensional volcanism (Pankhurst et al., 2000). The V1 pulse (188–178 Ma) is predominant in the North Patagonian Massif, V2 (172–162 Ma) defines the ages present in the Deseado Massif, and V3 (157–142 Ma) straddles the South Patagonian batholith. The Early and Middle Jurassic volcanic pulse (V1–V2; 188–178 Ma) has been proposed as a signature of extra-basinal sourcing due to its unique age range noted only in the region (Ghiglione et al., 2015). Zircon results from the Aptian–Albian fluvial units of the Chubut Group and Río Belgrano–Río Tarde Formations located within the North Patagonian Massif and west of the Deseado Massif in the northern depocenter of the basin, respectively, show that V1 stage volcanic rocks were the primary source for these Formations as well as 130–100 Ma grains representative of coeval volcanic ash fallout coincident with increased Andean arc activity (**Figure 10**; Ghiglione et al., 2015; Navarro et at., 2015). These age ranges thus may also represent some amount of recycling of exhumed volcaniclastic sequences near the northern margin of the basin (Ghiglione et al., 2015; Ghiglione et al., 2021). Metamorphic basement now exposed along the eastern flank of the Southern Patagonia Andes is covered by Late Jurassic (V3) volcanic rocks of the El Quemado, Ibañez and Tobífera Formations. Thus, presence of V3 stage aged grains with Paleozoic metamorphic material in the Cretaceous foreland may suggest Late Jurassic grains were largely recycled into the basin via tectonic unroofing and faulting along the basement thrust front associated with fold-and-thrust belt development (Ghiglione et al., 2015; Ghiglione et al., 2021).

4.6.3 Jurassic–Cretaceous Patagonia Arc and Batholith

The Andean Cordillera and South Patagonian batholith occupy the western margin of Patagonia. Arc magmatism ranges from 157 to 15 Ma, which is divided into four major pulses: 157–145 Ma (J), 144–137 Ma (K1), 136–127 Ma (K2), and 126–75 Ma (K3) (**Figure 8**; Hervé et al., 2007). Contemporaneous volcanism of the Andean arc (K3) makes up the majority of analyzed grains from both the La Anita and Alta Vista Formations (**Figure 8**).

4.7 Detrital Zircon Provenance of the Alta Vista Formation

Zircon age spectra from the Alta Vista Formation (N = 4; n = 1,159) are consistent with derivation from known terranes that sourced the Magallanes-Austral Basin during the Cretaceous. These include Paleozoic metamorphic and metasedimentary basement complexes and recycled Upper Jurassic V3 extensional volcanic rocks that represent exhumation of the basement domain via tectonic development of the fold-and-thrust along the eastern flank of the South Patagonian batholith (48% of total analyzed grains; 157–142 Ma; 310–260 Ma and older Paleozoic ages; Faúndez et al., 2002; Pankhurst et al., 2000; Hervé et al., 2003; Hervé et al., 2008; Hervé et al., 2010; **Figure 10**), Jurassic synrift volcanic rocks associated with distal sources of the Deseado and North

Patagonian Massifs to the north and northeast (2% of total analyzed grains; V1–V2: 188–162 Ma; Gust et al., 1985; Pankhurst et al., 1998; Pankhurst et al., 2000; Calderón et al., 2007; **Figure 10**), and Patagonian arc/batholith rocks that occupied the western Patagonia convergent margin (50% of total analyzed grains; 144–75 Ma; Hervé et al., 2007; **Figure 10**).

4.8 Detrital Zircon Provenance of the La Anita Formation

Similar to the Alta Vista Formation, detrital zircon data from the La Anita Formation (N = 16, n = 4,060) contain age ranges consistent with known source terranes for the Magallanes-Austral Basin (**Figure 8**). These include grains from recycled metamorphic basement complexes and overlying V3 extensional volcanic rocks (35% of total analyzed grains; Faúndez et al., 2002; Hervé et al., 2003; Hervé et al., 2008; Hervé et al., 2010; **Figure 10**), Jurassic extra-basinal volcanic terranes (4% of total analyzed grains; 188–162 Ma; Gust et al., 1985; Pankhurst et al., 1998; Pankhurst et al., 2000; Calderón et al., 2007; **Figure 10**), and the Patagonian arc and batholith (61% of all analyzed grains; 144–75 Ma; Hervé et al., 2007; **Figure 10**). General age distributions are in agreement with detrital zircon distributions from age equivalent strata analyzed by other workers (Sickmann et al., 2018; Sickmann et al., 2019; Ghiglione et al., 2021).

Detrital zircon from the La Anita Formation was primarily derived from the Cretaceous Patagonian volcanic arc and batholith, with secondary contributions from recycled grains from the foreland fold-and-thrust belt and Jurassic volcanic rocks (**Figure 8**). Jurassic zircons are likely sourced from V3 synrift volcanic units exposed along the Patagonian fold-and-thrust belt, as well as V1–V2 extensional volcanic rocks from the North Patagonian and Deseado Massifs (Pankhurst et al., 2000; Calderón et al., 2007). Paleozoic basement underlies the North Patagonian and Deseado Massifs, which may also provide some amount of sediment into the basement (Pankhurst et al., 2006; Chernicoff et al., 2013; Moreira et al., 2013). However, the co-appearance of Late Jurassic V3 grains with Paleozoic material suggests that the more proximal Paleozoic basement exposed along the fold-and-thrust belt is a more likely source for this age peak. Moreover, V1–V2 age peaks are in greater abundance in samples with a lesser amount of Paleozoic grains, suggesting it is less likely they are derivative of the same source area (e.g., LFA-5 samples, **Figure 8**). The presence of these age signals within the La Anita Formation suggests catchment sizes may have been large enough to source distal (hundreds of kms) sediments into the basin by Santonian–Campanian time, a finding observed in other Cretaceous, shallow-water strata in the region (e.g., Malkowski et al., 2017a; Schwartz et al., 2017; Sickmann et al., 2019). The presence of a distinct Early Jurassic peak at ca. 180 Ma unique to extra-basinal sources from the North Patagonian Massif indicates that some proportion of Jurassic sediment is far traveled (Ghiglione et al., 2015; Navarro et al., 2015). Alternatively, Early Jurassic ages may have been recycled from Aptian–Albian fluvial deposits that also contain 180 Ma grains located north of the terminus of the basin and west of the Deseado Massif, and north of the Golfo San Jorge Basin (**Figure 10**; Ghiglione et al., 2015).

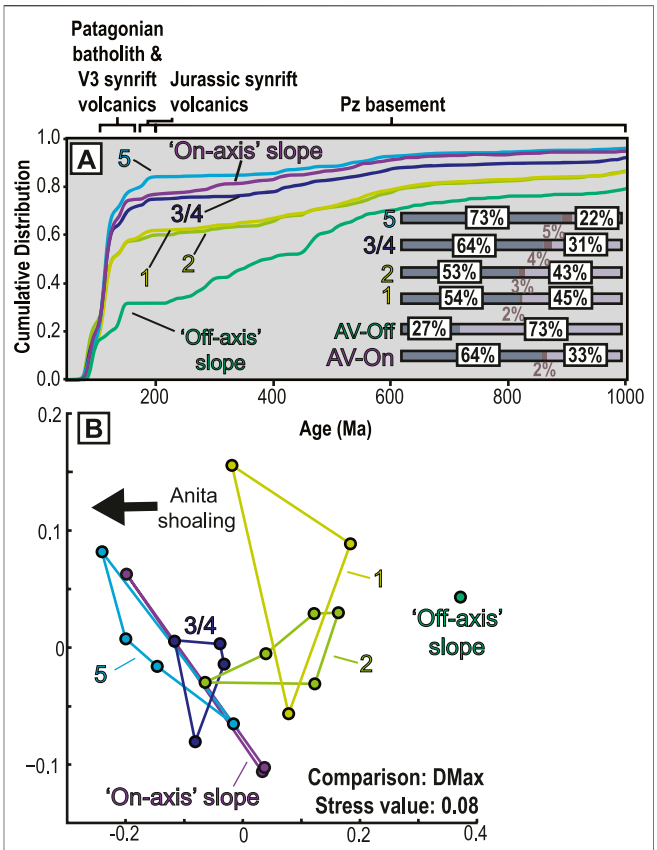

FIGURE 11 | (A) Cumulative frequency distributions of compiled detrital zircon data from the La Anita and Alta Vista Formations according to lithofacies association. Note the progressive increase in arc-derived material coincident with shoaling stratigraphy and whether or not the Alta Vista Formation grouping is representative of an "on-axis" or "off-axis" environment. **(B)** Multidimensional scaling plot using the DMax value of the K-S statistic of detrital zircon data from the Alta Vista and La Anita Formations grouped according to lithofacies association. Stress value = 0.08 (reasonable stress values are typically defined as <0.1; Kruskal, 1964). Note the grouping of lithofacies associations according to the interpreted similarity in depositional environments. Moreover, note that "on-axis" Alta Vista Formation samples group closer to LFA-5 and LFA-3/4 while the "off-axis" sample is closer to LFA-1 and LFA-2.

5 DISCUSSION

5.1 Depositional Controls on La Anita Detrital Zircon Provenance Signatures

To examine the relationship between lithofacies and detrital zircon spectra, we plot cumulative frequency and multidimensional scaling plots of the Alta Vista and La Anita Formation samples grouped by assigned lithofacies association (**Figure 11**). Binning these data according to interpreted depositional environment yields a provenance trend of

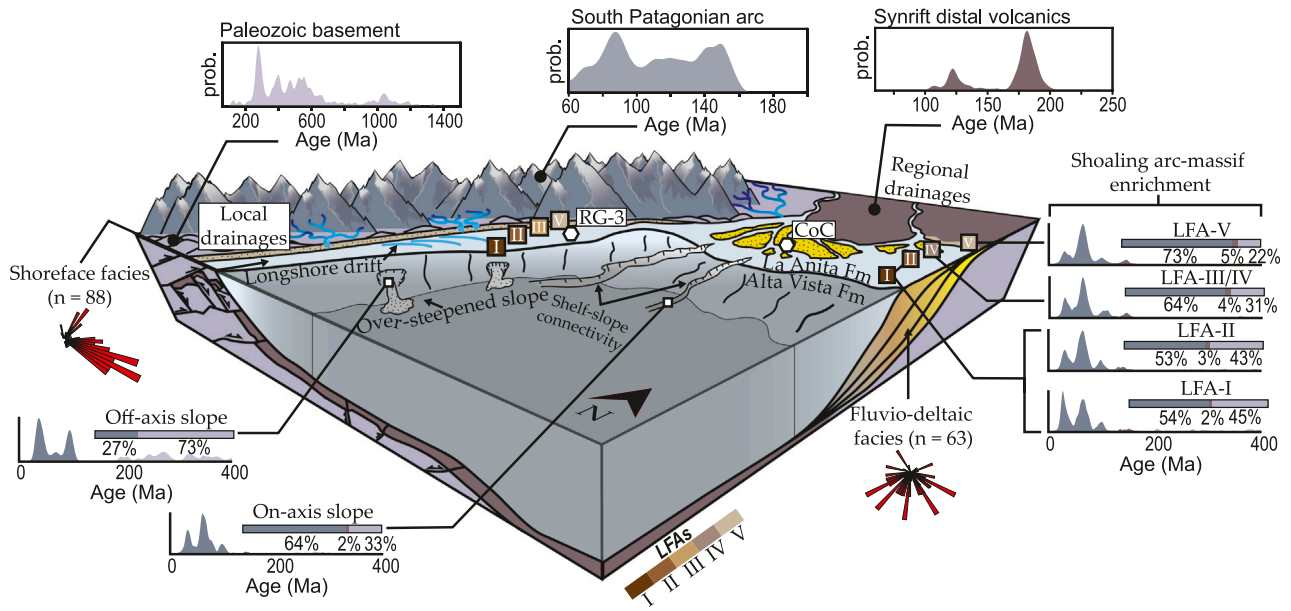

FIGURE 12 | Schematic depositional model for the Alta Vista and La Anita Formations and explanation for noted variation in detrital zircon age distributions in concert with change in depositional environments. Colored squares with labeled roman numerals are approximate locations of interpreted depositional environments from lithofacies associations. White hexagons are examples of approximate locations of measured stratigraphic sections from this study. Source regions are color-coded and labeled as deriving from either the Patagonian arc, Jurassic synrift volcanic materials from regional terranes, or Paleozoic basement uplifted along the Cretaceous orogenic front. Note that samples closer to the La Anita delta (in yellow) and shoreface (in tan) are able to more easily sequester sediment from regionally developed catchments tapping both the magmatic arc and distal sources. Moving down-section, the local fold-and-thrust belt signature becomes more pronounced, and distal sources diminish (see age distributions of LFA-1 and LFA-2 compared to LFA-3/4 and LFA-5). Paleocurrents from shoreface facies suggest that progressive longshore drift and shallow-marine transport processes may have been able to adequately move enough locally derived sediment to substantially dilute the fluvio-deltaic signature. For the Alta Vista Formation, note the markedly different age distributions between the on-axis and off-axis samples. Those from on-axis strata, rich in thick-bedded high density turbidites, were likely directly connected to the La Anita delta, which resulted in similar age distributions. Conversely, those portions of the Alta Vista Formation with no evidence of high rates of sedimentation may have been wholly isolated from the La Anita delta and thus only capable of transporting predominantly local sources.

increasing arc and distal massif-derived volcanic rock components and decreasing contributions from the recycled material derived from the exhumation of basement within the fold-and-thrust belt that correlates with shoaling of depositional environments (**Figure 11A**). Zircon spectra from LFA-1 and LFA-2 tend to have a lesser contribution from the Cretaceous Andes (LFA-1: 54%, LFA-2: 53%) and a moderate contribution from Paleozoic basement and overlying V3 volcanic rocks (LFA-1: 45%, LFA-2: 43%). Age distributions for LFA-3/4 and LFA-5, however, have a higher signal strength from the Cretaceous Andes (LFA-3/4: 64%, LFA-5: 73%) and a lesser contribution from the adjacent fold-and-thrust belt (LFA-3/4: 31%, LFA-5: 22%). We also note a 1–3% increase in the amount of V1–V2 peripheral volcanic sources from LFAs-3–5 when compared to LFA-1–2 (**Figure 11**). This trend is apparent in both the variation in compiled lithofacies datasets as cumulative frequency distributions and in the grouping of lithofacies associations in multidimensional scaling space (**Figures 11A,B**). We interpret this correlation as evidence for dynamic, competing erosion and transport processes and/or downstream dilution along the continental slope, shelf and shoreline, which yielded intraformational heterogeneity in detrital zircon sample age distributions.

Samples from the shallowest environments of the La Anita Formation (i.e., upper shoreface, foreshore, and delta front lithofacies) are the most arc-dominant (avg. ~69%; 144–75 Ma) and all contain ages associated with Early Jurassic V1–V2 volcanic rocks from extra-basinal terranes. Large, well-developed regional watersheds likely provided sediment from the nearby volcanic arc edifice and structural highs tapping far-traveled sediment from the Deseado and North Patagonian Massifs (**Figure 10**). Arc-derived zircon abundance decreases noticeably in samples from further offshore environments (i.e., lower shoreface/inner shelf and middle shoreface lithofacies; LFA-1, 2; avg. ~54% of all analyzed grains; **Figure 11**). Likewise, the amount of Paleozoic and Late Jurassic grains interpreted as being derived from the adjacent fold-and-thrust belt increases to an average of 44%. The progressive decrease in arc material and increase in fold-and-thrust belt zircon imply that enhanced shallow-marine erosive processes transporting local sediment and the increased distance from that La Anita delta, which provided regionally derived zircon, led to progressive downdip mixing between local and regional sources (**Figure 12**). Paleocurrent directions from lithofacies representative of offshore depositional environments and from regions more laterally distant from interpreted fluvio-

deltaic facies are predominantly to the southeast, with subordinate amounts to the northeast. Fluvio-deltaic facies record radial dispersion to the southwest, southeast and south (**Figures 4**; **12**). The bimodal dispersal pattern of further downdip facies may be indicative of offshore, marine currents redistributing sediment via wave or tidal actions whereas radial patterns broadly southward likely represent deposition via distributary channels of a delta (Selley, 1968; Miall, 1978; **Figure 7**). Offshore facies may have been progressively susceptible to reworking via marine currents that delivered local, fold-and-thrust belt derived sediment from the northwest into the basin. Thus, while these lithofacies were deposited contemporaneously and in proximal distance to each other, the relative source abundances varied markedly as a function of competition between fluvio-deltaic transport and subsequent reworking via shallow-marine transport processes.

5.2 Shallow to Deep-Water Sediment Pathway Connectivity and Provenance Records

The proximity to La Anita delta facies appears to also contribute to detrital zircon variability in continental slope facies of the Alta Vista Formation. Sample RG-01 from the Alta Vista Formation is a part of a mud-rich section of interstratified mudstone and thin-bedded, fine-grained turbidite deposits (**Figure 9A**). No channelized units, major erosive beds, thick-bedded sandstone beds, or channel-levee systems were noted in this region. Calculated aggradation rates from ash ages of this section were relatively low (34 m Myr^{-1}; see **Section 4.3.1**). We interpret section AV-1 as being off-axis from the locus of a sedimentation, such as an unincised portion of the continental slope (**Figure 12**). Conversely, the samples from section CM contain large, thick-bedded sandstone beds, which are amalgamated and several meters thick towards the top of the section (**Figure 9D**). These units are locally isoclinally folded, which we interpret as synsedimentary folds due to slumping and sliding on oversteepened portions of the continental slope (**Figures 9C–E**). We therefore argue that section CM represents a portion of continental slope proximal to, or a part of, an on-axis, deep-water channel system or shelf-edge delta front that received high amounts of sediment from the La Anita delta. Sample RG-01 from section AV-1 is primarily made up of Paleozoic basement and Late Jurassic grains derived from the fold-and-thrust belt (~73% of all analyzed grains; **Figures 8**, **12**). This suggests that the primary source for sample RG-01 was from local, small-area drainages tapping the adjacent uplifted basement within the Cretaceous fold-and-thrust belt. Notably, this sample contains no zircon grains attributed to V1–V2 distal massif sources. This indicates that the La Anita delta may not have contributed sediment to this portion of the continental slope. Instead, "off-axis" portions of the slope received sediment from slope failures that only contained locally derived sediment. Conversely, the samples from section CM (**Figure 2**; **Figures 9B–E**) have zircon distributions most similar to the shallow-water environments from the La Anita Formation (**Figure 8**; **Figure 11**). This marked variation between the sandier and muddier portions of the Alta Vista Formation highlights the impact of fluvio-deltaic connectivity to the continental slope on resulting provenance signatures. Given the large number of amalgamated sand beds making up section CM, we argue that this section was likely proximal to the sand-rich La Anita shelf-edge delta or deposited near a submarine canyon system (**Figure 12**). In either scenario, these samples support the hypothesis that portions of the continental slope and shelf that were down paleoslope of the primary depositional pathway of the La Anita fluvio-deltaic system had direct connectivity to its onshore counterparts via canyon incision onto the continental shelf (e.g., Monterey Canyon, California; Paull et al., 2011) or progradation of the La Anita shelf-edge delta (e.g., Dorotea-Tres Pasos Formations; Hubbard et al., 2010; Schwartz and Graham, 2015). An alternative explanation for the systematic variation in detrital zircon spectra along depositional gradient is grain-size biasing (e.g., Lawrence et al., 2011; Ibañez-Mejia et al., 2018; Cantine et al., 2021). Although grain-size dependent processes may influence resulting detrital zircon deposition, we have mitigated this potential complication via sampling sandstone beds ranging from fine to lower-medium grained sand. Moreover, recent work by Leary et al. (2020) demonstrates that grain size and detrital zircon spectra are not significantly correlated. Instead, the relative input between distally derived sources and local uplifts appeared to exert a stronger control on resulting zircon distributions. A more detailed study that incorporates grain size analysis with detrital zircon work is necessary to further detail this potential complication.

6 CONCLUSION

We pair lithofacies analysis with a high-N detrital zircon sampling effort of the Upper Cretaceous Alta Vista and La Anita Formations to examine the relationships between depositional environments and provenance data. This study focuses on an outcrop belt in the Zona Centro region of the Austral sector of the Magallanes-Austral Basin. Lithofacies results from this region suggest that the La Anita Formation is composed of a progradational sequence of shallow to marginal marine environments that range from inner shelf to foreshore deposits. Lateral facies variation across the region indicates that the La Anita Formation records variable influence of a fluvially dominant delta system towards the eastern portion of the outcrop belt, while western sections are representative of deposition onto an open, storm-influenced shoreface. Paleocurrent data record competing longshore, shallow-marine and deltaic transport processes that resulted in variable sediment dispersal pathways broadly to the south and southeast.

Detrital zircon data from the La Anita Formation record a shift from sourcing by established regional drainages to mixing

with locally derived sediments from the adjacent fold-and-thrust belt. This progressive change in zircon age distribution is coincident with changing shallow-marine facies patterns from foreshore to offshore environments. We speculate that this correlation demonstrates that provenance results can vary greatly within a single Formation due to the dynamics of competing transport and erosion processes across a source-to-sink system. Combining these data with detrital zircon results from the continental slope facies of the Alta Vista Formation suggest that muddier portions of the continental slope were disconnected from the coeval sediment dispersal pathways of the La Anita delta. Instead, these sediments recycled local sediment through re-entrainment of material on the continental slope and shelf via mass transport deposits and sediment gravity flows. Conversely, portions of the Alta Vista Formation that were proximal to the point sources of sediment mimicked the provenance distribution of the shallow-water equivalents of the La Anita Formation. This suggests that connectivity to shallow-marine sources via submarine canyon incision or proximity to a shelf-edge delta is necessary for provenance signals to propagate down system to their ultimate ocean basin sinks.

Using a combination of maximum depositional ages from detrital zircon samples and ash ages collected from the Alta Vista Formation, we constrain the timing of deposition of the Alta Vista and La Anita Formations to the late Turonian through Campanian. This age range is consistent with the most recent chronostratigraphic framework for the deposition of the Cerro Toro Formation in the Magallanes sector of the basin.

DATA AVAILABILITY STATEMENT

The original contributions presented in the study are included in the article/**Supplementary Material**, further inquiries can be directed to the corresponding author.

AUTHOR CONTRIBUTIONS

SD: Writing, field work, data acquisition, figure drafting, discussion/interpretation MM: Editing, field work, data acquisition, discussion/interpretation TS: Editing, field work, data acquisition, discussion/interpretation ZS: Editing, field work, discussion/interpretation SG: Editing, discussion/interpretation

FUNDING

This research was funded by Stanford University and the Stanford Project on Deep-water Depositional Systems (SPODDS), an industry consortium that has included Anadarko, Chevron, ConocoPhillips, RAG Austria AG, Aramco, Shell, Aera Energy, Matador, and YPF.

ACKNOWLEDGMENTS

Thank you to field assistants Mark Raftrey and Tom Boag. We are grateful to George Gehrels, Mark Pecha, and the staff at the University of Arizona Laserchron Center which includes support from NSF-EAR grants 1649254 and 2050246. Thank you to Katie Dunn for her help with heavy mineral separations. The contents and structuring of the manuscript were greatly improved by reviews from Matías Ghiglione and Maximiliano Naipauer, and U.S. Geological Survey internal reviews by Marieke Dechesne and Natalie Latysh. Any use of trade, firm, or product names is for descriptive purposes only and does not imply endorsement by the U.S. Government.

SUPPLEMENTARY MATERIAL

The Supplementary Material for this article can be found online at: https://www.frontiersin.org/articles/10.3389/feart.2022.824930/full#supplementary-material

REFERENCES

Alabaster, T., and Storey, B. C. (1990). Modified Gulf of California Model for South Georgia, North Scotia Ridge, and Implications for the Rocas Verdes Back-Arc Basin, Southern Andes. *Geology* 18, 597–500. Available at: http://pubs.geoscienceworld.org/gsa/geology/article-pdf/18/6/497/3512056/i0091-7613-18-6-497.pdf. doi:10.1130/0091-7613(1990)018<0497:mgocmf>2.3.co;2

Allen, R. B. (1982). *Geología de la Cordillera Sarmiento, Andes Patagonicos, entre los 51°00' y 52°15' Lat. S., Magallanes, Chile*. Santiago: Servicio Nacional de Geología y Minería Boletin, 38, 46.

Aramendía, I., Ramos, M. E., Geuna, S., Cuitiño, J. I., and Ghiglione, M. C. (2018). A Multidisciplinary Study of the Lower Cretaceous Marine to Continental Transition in the Northern Austral-Magallanes Basin and its Geodynamic Significance. *J. S. Am. Earth Sci.* 86, 54–69. doi:10.1016/j.jsames.2018.06.010

Arbe, H. A. (2002). "Análisis estratigráfico del Cretácico de la cuenca Austral (Stratigraphic analysis of the Cretaceous of the Austral Basin)," in Geología y Recursos Naturales de *Santa Cruz*. Editor M. J. Haller (Buenos Aires, Argentina, El Calafate: Relatario del 15th Congreso Geológico Argentino), 103–128.

Arbe, H. A., and Hechem, J. J. (1984). "Estratigrafia y facies de depósitos continentals, litorales, y marinos del Cretàcico superior, Lago Argentino," in *Actas 9 Congreso Geológico Argentino* (Bariloche, Argentina: Congreso Geologico Argentino), 124–158.

Armitage, D. A., Romans, B. W., Covault, J. A., and Graham, S. A. (2009). The Influence of Mass-Transport-Deposit Surface Topography on the Evolution of Turbidite Architecture: The Sierra Contreras, Tres Pasos Formation (Cretaceous), Southern Chile. *J. Sediment. Res.* 79, 287–301. doi:10.2110/JSR.2009.035

Bernhardt, A., Jobe, Z. R., Grove, M., and Lowe, D. R. (2012). Palaeogeography and Diachronous Infill of an Ancient Deep-Marine Foreland Basin, Upper Cretaceous Cerro Toro Formation, Magallanes Basin. *Basin Res.* 24, 269–294. doi:10.1111/j.1365-2117.2011.00528.x

Bhattacharya, J. P. (2010). "Deltas," in *Facies Models 4*. Editors R. W. Dalrymple and N. P. James (St. John's, Canada: Geological Association of Canada), 233–264.

Calderón, M., Fildani, A., Hervé, F., Fanning, C. M., Weislogel, A., and Cordani, U. (2007). Late Jurassic Bimodal Magmatism in the Northern Sea-Floor Remnant of the Rocas Verdes Basin, Southern Patagonian Andes. *J. Geol. Soc. Lond.* 164, 1011–1022. doi:10.1144/0016-76492006-102

Calderón, M., Prades, C. F., Hervé, F., Avendaño, V., Fanning, C. M., Massonne, H.-J., et al. (2013). Petrological Vestiges of the Late Jurassic-Early Cretaceous Transition from Rift to Back-Arc Basin in Southernmost Chile: New Age and Geochemical Data from the Capitán Aracena, Carlos III, and Tortuga

Ophiolitic Complexes. *Geochem. J.* 47, 201–217. doi:10.2343/GEOCHEMJ.2.0235

Calderón, M., Hervé, F., Fuentes, F., Fosdick, J. C., Sepúlveda, F., and Galaz, G. (2016). "Tectonic Evolution of Paleozoic and Mesozoic Andean Metamorphic Complexes and the Rocas Verdes Ophiolites in Southern Patagonia," in *Geodynamic Evolution of the Southernmost Andes*. Editor M. C. Ghiglione (Springer Earth System Sciences), 7–36. doi:10.1007/978-3-319-39727-6_2

Cantine, M. D., Setera, J. B., Vantongeren, J. A., Mwinde, C., and Bergmann, K. D. (2021). Grain Size and Transport Biases in an Ediacaran Detrital Zircon Record. *J. Sediment. Res.* 91, 913–928. doi:10.2110/JSR.2020.153

Carvajal, C., Steel, R., and Petter, A. (2009). Sediment Supply: The Main Driver of Shelf-Margin Growth. *Earth-Science Rev.* 96, 221–248. doi:10.1016/J.EARSCIREV.2009.06.008

Cawood, P. A., Nemchin, A. A., Freeman, M., and Sircombe, K. (2003). Linking Source and Sedimentary Basin: Detrital Zircon Record of Sediment Flux along a Modern River System and Implications for Provenance Studies. *Earth Planet. Sci. Lett.* 210, 259–268. doi:10.1016/S0012-821X(03)00122-5

Cawood, P. A., Nemchin, A. A., Strachan, R., Prave, T., and Krabbendam, M. (2007). Sedimentary Basin and Detrital Zircon Record along East Laurentia and Baltica during Assembly and Breakup of Rodinia. *J. Geol. Soc. Lond.* 164, 257–275. doi:10.1144/0016-76492006-115

Chernicoff, C. J., Zappettini, E. O., Santos, J. O. S., McNaughton, N. J., and Belousova, E. (2013). Combined U-Pb SHRIMP and Hf Isotope Study of the Late Paleozoic Yaminué Complex, Rio Negro Province, Argentina: Implications for the Origin and Evolution of the Patagonia Composite Terrane. *Geosci. Front.* 4, 37–56. doi:10.1016/J.GSF.2012.06.003

Clifton, H. E. (2006). *A Reexamination of Facies Models for Clastic Shorelines*, 4. Tulsa, Oklahoma: SEPM Special Publication, 293–337. doi:10.2110/pec.06.84.0293

Clifton, H. E. (1969). Beach Lamination: Nature and Origin. *Mar. Geol.* 7, 553–559. doi:10.1016/0025-3227(69)90023-1

Collinson, J. D. (1969). The Sedimentology of the Grindslow Shales and the Kinderscout Grit: A Deltaic Complex in the Namurian of Northern England. *J. Sediment. Res.* 39, 194–221. doi:10.1306/74D71C17-2B21-11D7-8648000102C1865D

Coutts, D. S., Matthews, W. A., and Hubbard, S. M. (2019). Assessment of Widely Used Methods to Derive Depositional Ages from Detrital Zircon Populations. *Geosci. Front.* 10, 1421–1435. doi:10.1016/j.gsf.2018.11.002

Crane, W. H., and Lowe, D. R. (2008). Architecture and Evolution of the Paine Channel Complex, Cerro Toro Formation (Upper Cretaceous), Silla Syncline, Magallanes Basin, Chile. *Sedimentology* 55, 979–1009. doi:10.1111/J.1365-3091.2007.00933.X

Dalziel, I. W. D. (1986). Collision and Cordilleran Orogenesis: An Andean Perspective. *Geol. Soc. Lond. Spec. Publ.* 19, 389–404. doi:10.1144/GSL.SP.1986.019.01.22

Dalziel, I. W. D., de Wit, M. J., and Palmer, K. F. (1974). Fossil Marginal Basin in the Southern Andes. *Nature* 250, 291–294. doi:10.1038/250291a0

Daniels, B. G., Auchter, N. C., Hubbard, S. M., Romans, B. W., Matthews, W. A., and Stright, L. (2018). Timing of Deep-Water Slope Evolution Constrained by Large-N Detrital and Volcanic Ash Zircon Geochronology, Cretaceous Magallanes Basin, Chile. *Bull. Geol. Soc. Am.* 130, 438–454. doi:10.1130/B31757.1

Daniels, B. G., Hubbard, S. M., Romans, B. W., Malkowski, M. A., Matthews, W. A., Bernhardt, A., et al. (2019). Revised Chronostratigraphic Framework for the Cretaceous Magallanes-Austral Basin, Última Esperanza Province, Chile. *J. South Am. Earth Sci.* 94, 102209. doi:10.1016/j.jsames.2019.05.025

de Wit, M. J., and Stern, C. R. (1981). Variations in the Degree of Crustal Extension during Formation of a Back-Arc Basin. *Tectonophysics* 72, 229–260. doi:10.1016/0040-1951(81)90240-7

DeCelles, P. G., Gehrels, G. E., Najman, Y., Martin, A. J., Carter, A., and Garzanti, E. (2004). Detrital Geochronology and Geochemistry of Cretaceous-Early Miocene Strata of Nepal: Implications for Timing and Diachroneity of Initial Himalayan Orogenesis. *Earth Planet. Sci. Lett.* 227, 313–330. doi:10.1016/j.epsl.2004.08.019

DeGraaff-Surpless, K., Mahoney, J. B., Wooden, J. L., and McWilliams, M. O. (2003). Lithofacies Control in Detrital Zircon Provenance Studies: Insights from the Cretaceous Methow Basin, Southern Canadian Cordillera. *Bull. Geol. Soc. Am.* 115, 899–915. doi:10.1130/B25267.1

Dickinson, W. R., and Gehrels, G. E. (2009). Use of U-Pb Ages of Detrital Zircons to Infer Maximum Depositional Ages of Strata: A Test against a Colorado Plateau Mesozoic Database. *Earth Planet. Sci. Lett.* 288, 115–125. doi:10.1016/J.EPSL.2009.09.013

Dumas, S., and Arnott, R. W. C. (2006). Origin of Hummocky and Swaley Cross-Stratification- The Controlling Influence of Unidirectional Current Strength and Aggradation Rate. *Geology* 34, 1073–1076. doi:10.1130/G22930A.1

Dumas, S., Arnott, R. W. C., and Southard, J. B. (2005). Experiments on Oscillatory-Flow and Combined-Flow Bed Forms: Implications for Interpreting Parts of the Shallow-Marine Sedimentary Record. *J. Sediment. Res.* 75 (3), 501–513, doi:10.2110/jsr.2005.039

Faúndez, V., Hervé, F., and Lacassie, J. P. (2002). Provenance and Depositional Setting of pre-Late Jurassic Turbidite Complexes in Patagonia, Chile. *New zeal. J. Geol. Geophys.* 45, 411–425. doi:10.1080/00288306.2002.9514982

Fedo, C. M., Sircombe, K. N., and Rainbird, R. H. (2003). Detrital Zircon Analysis of the Sedimentary Record. *Rev. Mineral. Geochem.* 53, 277–303. doi:10.2113/0530277

Fildani, A., Cope, T. D., Graham, S. A., and Wooden, J. L. (2003). Initiation of the Magallanes Foreland Basin: Timing of the Southernmost Patagonian Andes Orogeny Revised by Detrital Zircon Provenance Analysis. *Geology* 31, 1081–1084. doi:10.1130/G20016.1

Fildani, A., and Hessler, A. M. (2005). Stratigraphic Record across a Retroarc Basin Inversion: Rocas Verdes-Magallanes Basin, Patagonian Andes, Chile. *Bull. Geol. Soc. Am.* 117, 1596–1614. doi:10.1130/B25708.1

Finzel, E. S., Ridgway, K. D., and Trop, J. M. (2015). Provenance Signature of Changing Plate Boundary Conditions along a Convergent Margin: Detrital Record of Spreading-Ridge and Flat-Slab Subduction Processes, Cenozoic Forearc Basins, Alaska. *Geosphere* 11, 823–849. doi:10.1130/GES01029.1

Fosdick, J. C., Romans, B. W., Fildani, A., Bernhardt, A., Calderon, M., and Graham, S. A. (2011). Kinematic Evolution of the Patagonian Retroarc Fold-And-Thrust Belt and Magallanes Foreland Basin, Chile and Argentina, 51 30'S. *Geol. Soc. Am. Bull.* 123, 1679–1698. doi:10.1130/b30242.1

Garzanti, E., Andò, S., and Vezzoli, G. (2009). Grain-size Dependence of Sediment Composition and Environmental Bias in Provenance Studies. *Earth Planet. Sci. Lett.* 277, 422–432. doi:10.1016/J.EPSL.2008.11.007

Gehrels, G. E. (2000). Introduction to Detrital Zircon Studies of Paleozoic and Triassic Strata in Western Nevada and Northern California. *Spec. Pap. Geol. Soc. Am.* 347, 1–17. doi:10.1130/0-8137-2347-7.1

Gehrels, G. E., Valencia, V. A., Ruiz, J., Gehrels, G. E., Valencia, V. A., and Ruiz, J. (2008). Enhanced Precision, Accuracy, Efficiency, and Spatial Resolution of U-Pb Ages by Laser Ablation-Multicollector-Inductively Coupled Plasma-Mass Spectrometry. *Geochem. Geophys. Geosyst.* 9, 1–13. doi:10.1029/2007GC001805

Gehrels, G., and Pecha, M. (2014). Detrital Zircon U-Pb Geochronology and Hf Isotope Geochemistry of Paleozoic and Triassic Passive Margin Strata of Western North America. *Geosphere* 10, 49–65. doi:10.1130/GES00889.1

Ghiglione, M. C., Likerman, J., Barberón, V., Beatriz Giambiagi, L., Aguirre-Urreta, B., and Suarez, F. (2014). Geodynamic Context for the Deposition of Coarse-Grained Deep-Water Axial Channel Systems in the Patagonian Andes. *Basin Res.* 26, 726–745. doi:10.1111/bre.12061

Ghiglione, M. C., Naipauer, M., Sue, C., Barberón, V., Valencia, V., Aguirre-Urreta, B., et al. (2015). U-Pb Zircon Ages from the Northern Austral Basin and Their Correlation with the Early Cretaceous Exhumation and Volcanism of Patagonia. *Cretac. Res.* 55, 116–128. doi:10.1016/j.cretres.2015.02.006

Ghiglione, M. C., Rocha, E., Raggio, M. F., Ramos, M. E., Ronda, G., Moyano-Paz, D., et al. (2021). Santonian-Campanian Continentalization in the Austral-Magallanes Basin: Regional Correlation, Provenance and Geodynamic Setting. *Cretac. Res.* 128, 104968. doi:10.1016/j.cretres.2021.104968

Gooley, J. T., Grove, M., and Graham, S. A. (2021). "Tectonic Evolution of the Central California Margin as Reflected by Detrital Zircon Composition in the Mount Diablo Region," in *Regional Geology of Mount Diablo, California: Its Tectonic Evolution on the North America Plate Boundary*. Editors R. Sullivan, D. Sloan, J. R. Unruh, and D. P. Schwartz (Boulder, CO: Geological Society of America Memoir 217). doi:10.1130/2021.1217(14)

Gust, D. A., Biddle, K. T., Phelps, D. W., and Uliana, M. A. (1985). Associated Middle to Late Jurassic Volcanism and Extension in Southern South America. *Tectonophysics* 116, 223–253. doi:10.1016/0040-1951(85)90210-0

Hervé, F., Calderón, M., and Faúndez, V. (2008). The Metamorphic Complexes of the Patagonian and Fuegian Andes. *Geol. Acta* 6 (1), 43–53. Available at: https://revistes.ub.edu/index.php/GEOACTA/article/view/105.000000240. doi:10.1344/105.000000240

Hervé, F., Fanning, C. M., and Pankhurst, R. J. (2003). Detrital Zircon Age Patterns and Provenance of the Metamorphic Complexes of Southern Chile. *J. South Am. Earth Sci.* 16, 107–123. doi:10.1016/S0895-9811(03)00022-1

Hervé, F., Fanning, C. M., Pankhurst, R. J., Mpodozis, C., Klepeis, K., Calderón, M., et al. (2010). Detrital Zircon SHRIMP U-Pb age Study of the Cordillera Darwin Metamorphic Complex of Tierra del Fuego: Sedimentary Sources and Implications for the Evolution of the Pacific Margin of Gondwana. *J. Geol. Soc. Lond.* 167, 555–568. doi:10.1144/0016-76492009-124

Hervé, F., Pankhurst, R. J., Fanning, C. M., Calderón, M., and Yaxley, G. M. (2007). The South Patagonian Batholith: 150 My of Granite Magmatism on a Plate Margin. *Lithos* 97, 373–394. doi:10.1016/J.LITHOS.2007.01.007

Hervé, F., and Fanning, C. M. (2001). Late Triassic Detrital Zircons in Metaturbidites of the Chonos Metamorphic Complex, Southern Chile. *Revista Geológica de Chile* 28 (1), 91–104. doi:10.4067/S0716-02082001000100005

Hubbard, S. M., Fildani, A., Romans, B. W., Covault, J. A., and McHargue, T. R. (2010). High-Relief Slope Clinoform Development: Insights from Outcrop, Magallanes Basin, Chile. *J. Sediment. Res.* 80, 357–375. doi:10.2110/JSR.2010.042

Hubbard, S. M., Romans, B. W., and Graham, S. A. (2008). Deep-Water Foreland Basin Deposits of the Cerro Toro Formation, Magallanes Basin, Chile: Architectural Elements of a Sinuous Basin Axial Channel Belt. *Sedimentology* 55, 1333–1359. doi:10.1111/J.1365-3091.2007.00948.X

Ibañez-Mejia, M., Pullen, A., Pepper, M., Urbani, F., Ghoshal, G., and Ibañez-Mejia, J. C. (2018). Use and Abuse of Detrital Zircon U-Pb Geochronology-A Case from the Río Orinoco Delta, Eastern Venezuela. *Geology* 46, 1019–1022. doi:10.1130/G45596.1

Kraemer, E., and Riccardi, A. C. (1997). Estratigrafía de la región comprendida entre los lagos Argentino y Viedma (49°40′–50°10′ lat. S). *Prov. St. Cruz Rev. Asoc. Geol. Argent.* 52, 333–360.

Kruskal, J. B. (1964). Multidimensional Scaling by Optimizing Goodness of Fit to a Nonmetric Hypothesis. *Psychometrika* 29, 1–27. doi:10.1007/bf02289565

Lacovara, K. J., Lamanna, M. C., Ibiricu, L. M., Poole, J. C., Schroeter, E. R., Ullmann, P. V., et al. (2014). A Gigantic, Exceptionally Complete Titanosaurian Sauropod Dinosaur from Southern Patagonia, Argentina. *Sci. Rep.* 4, 6196. doi:10.1038/srep06196

Lawrence, R. L., Cox, R., Mapes, R. W., and Coleman, D. S. (2011). Hydrodynamic Fractionation of Zircon Age Populations. *Bull. Geol. Soc. Am.* 123, 295–305. doi:10.1130/B30151.1

Leary, R. J., Smith, M. E., and Umhoefer, P. (2020). Grain-Size Control on Detrital Zircon Cycloprovenance in the Late Paleozoic Paradox and Eagle Basins, USA. *J. Geophys. Res. Solid Earth* 125, e2019JB019226. doi:10.1029/2019JB019226

Leckie, D. A., and Walker, R. G. (1982). Storm- and Tide-Dominated Shorelines in Cretaceous Moosebar-Lower Gates Interval—Outcrop Equivalents of Deep Basin Gas Trap in Western Canada: Reply. *Am. Assoc. Pet. Geol. Bull.* 66, 2683–2684. doi:10.1306/03B5ACA0-16D1-11D7-8645000102C1865D

Lowe, D. R. (1982). Sediment Gravity Flows: II Depositional Models with Special Reference to the Deposits of High-Density Turbidity Currents. *J. Sediment. Res.* 52, 279–297. doi:10.1306/212F7F31-2B24-11D7-8648000102C1865D

MacEachern, J. A., Pemberton, S. G., Gingras, M. K., and Bann, K. L. (2010). "Ichnology and Facies Models," in *Facies Models 4*. Editors R.G. Dalrymple and N.P. James (St. John's, Canada: Geological Association of Canada), 19–58.

Macellari, C. E., Barrio, C. A., and Manassero, M. J. (1989). Upper Cretaceous to Paleocene Depositional Sequences and Sandstone Petrography of Southwestern Patagonia (Argentina and Chile). *J. South Am. Earth Sci.* 2, 223–239. doi:10.1016/0895-9811(89)90031-X

Malkowski, M. A., Grove, M., and Graham, S. A. (2016). Unzipping the Patagonian Andes-Long-Lived Influence of Rifting History on Foreland Basin Evolution. *Lithosphere* 8, 23–28. doi:10.1130/L489.1

Malkowski, M. A., Jobe, Z. R., Sharman, G. R., and Graham, S. A. (2018). Downslope Facies Variability within Deep-Water Channel Systems: Insights from the Upper Cretaceous Cerro Toro Formation, Southern Patagonia. *Sedimentology* 65, 1918–1946. doi:10.1111/sed.12452

Malkowski, M. A., Schwartz, T. M., Sharman, G. R., Sickmann, Z. T., and Graham, S. A. (2017a). Stratigraphic and Provenance Variations in the Early Evolution of the Magallanes-Austral Foreland Basin: Implications for the Role of Longitudinal versus Transverse Sediment Dispersal during Arc-Continent Collision. *Bull. Geol. Soc. Am.* 129, 349–371. doi:10.1130/B31549.1

Malkowski, M. A., Sharman, G. R., Graham, S. A., and Fildani, A. (2017b). Characterisation and Diachronous Initiation of Coarse Clastic Deposition in the Magallanes-Austral Foreland Basin, Patagonian Andes. *Basin Res.* 29, 298–326. doi:10.1111/bre.12150

Malkowski, M. A., Sharman, G. R., Johnstone, S. A., Grove, M. J., Kimbrough, D. L., and Graham, S. A. (2019). Dilution and Propagation of Provenance Trends in Sand and Mud: Geochemistry and Detrital Zircon Geochronology of Modern Sediment from Central California (U.S.A.). *Am. J. Sci.* 319, 846–902. doi:10.2475/10.2019.02

Miall, A. D. (1978). "Paleocurrent Analysis," in *Sedimentology*. Berlin/Heidelberg, Germany, 825–830. doi:10.1007/978-1-4020-3609-5_152

Moecher, D., and Samson, S. (2006). Differential Zircon Fertility of Source Terranes and Natural Bias in the Detrital Zircon Record: Implications for Sedimentary Provenance Analysis. *Earth Planet. Sci. Lett.* 247, 252–266. doi:10.1016/J.EPSL.2006.04.035

Moreira, P., Fernández, R., Hervé, F., Fanning, C. M., and Schalamuk, I. A. (2013). Detrital Zircons U-Pb SHRIMP Ages and Provenance of La Modesta Formation, Patagonia Argentina. *J. South Am. Earth Sci.* 47, 32–46. doi:10.1016/J.JSAMES.2013.05.010

Moyano Paz, D., Richiano, S., Varela, A. N., Gómez Dacál, A. R., and Poiré, D. G. (2020). Ichnological Signatures from Wave- and Fluvial-Dominated Deltas: The La Anita Formation, Upper Cretaceous, Austral-Magallanes Basin, Patagonia. *Mar. Pet. Geol.* 114, 104168. doi:10.1016/j.marpetgeo.2019.104168

Moyano Paz, D., Tettamanti, C., Varela, A. N., Cereceda, A., and Poiré, D. G. (2018). Depositional Processes and Stratigraphic Evolution of the Campanian Deltaic System of La Anita Formation, Austral-Magallanes Basin, Patagonia, Argentina. *Lat. Am. J. Sedimentol. Basin Anal.* 25, 69–92.

Natland, M. L., Eduardo, G. P., Canon, A., and Ernst, M. (1974). *A System of Stages for Correlation of Magallanes Basin Sediments*, 139. Boulder, CO: Geological Society of America, 126. doi:10.1130/MEM139

Navarro, E. L., Astini, R. A., Belousova, E., Guler, M. V., and Gehrels, G. (2015). Detrital Zircon Geochronology and Provenance of the Chubut Group in the Northeast of Patagonia, Argentina. *J. South Am. Earth Sci.* 63, 149–161. doi:10.1016/J.JSAMES.2015.07.006

Novas, F. E., Ezcurra, M. D., and Lecuona, A. (2008). Orkoraptor burkei nov. gen. et sp., a large theropod from the Maastrichtian Pari Aike Formation, Southern Patagonia, Argentina. *Cretac. Res.* 29, 468–480. doi:10.1016/J.CRETRES.2008.01.001

Olariu, C., and Bhattacharya, J. P. (2006). Terminal Distributary Channels and Delta Front Architecture of River-Dominated Delta Systems. *J. Sediment. Res.* 76, 212–233. doi:10.2110/jsr.2006.026

Pankhurst, R. J., Rapela, C. W., Fanning, C. M., and Márquez, M. (2006). Gondwanide Continental Collision and the Origin of Patagonia. *Earth-Sci. Rev.* 76, 235–257. doi:10.1016/J.EARSCIREV.2006.02.001

Pankhurst, R. J., Riley, T. R., Fanning, C. M., and Kelley, S. P. (2000). Episodic Silicic Volcanism in Patagonia and the Antarctic Peninsula: Chronology of Magmatism Associated with the Break-Up of Gondwana. *J. Pet.*. 41, 605–625. doi:10.1093/PETROLOGY/41.5.605

Pankhurst, R. J., Leat, P. T., Sruoga, P., Rapela, C. W., Márquez, M., Storey, B. C., and Riley, T. R. (1998). The Chon Aike province of Patagonia and Related Rocks in West Antarctica: A Silicic Large Igneous Province. *J. Volcanol. Geotherm. Res.* 81 (1–2), 113–136. doi:10.1016/S0377-0273(97)00070-X

Paull, C. K., Caress, D. W., Ussler, W., Lundsten, E., and Meiner-Johnson, M. (2011). High-Resolution Bathymetry of the Axial Channels within Monterey and Soquel Submarine Canyons, Offshore Central California. *Geosphere* 7, 1077–1101. doi:10.1130/GES00636.1

Plint, A. G. (2010). "Wave- and Storm-Dominated Shoreline and Shallow-Marine Systems," in *Facies Models 4*. Editors R.W. Dalrymple and N.P. James (St. John's, Canada: Geological Association of Canada), 167–200.

Ramos, V. A. (1989). Andean Foothills Structures in Northern Magallanes Basin, Argentina. *Am. Assoc. Pet. Geol. Bull.* 73, 887–903. Available at: http://pubs.geoscienceworld.org/aapgbull/article-pdf/73/7/887/4470514/aapg_1989_0073_0007_0887.pdf. doi:10.1306/44b4a28a-170a-11d7-8645000102c1865d

Riccardi, A. C., and Rolleri, E. O. (1980). "Cordillera Patagonica Austral," in *Segundo Simposio de Geología Regional Argentina* (Cordoba, Argentine: Segundo Simposio de Geologıa Regional Argentina), 2, 1163–1306.

Romans, B. W., Fildani, A., Graham, S. A., Hubbard, S. M., and Covault, J. A. (2010). Importance of Predecessor Basin History on Sedimentary Fill of a Retroarc Foreland Basin: Provenance Analysis of the Cretaceous Magallanes Basin, Chile (50-52°S). *Basin Res.* 22, 640–658. doi:10.1111/J.1365-2117.2009.00443.X

Romans, B. W., Hubbard, S. M., and Graham, S. A. (2009). Stratigraphic Evolution of an Outcropping Continental Slope System, Tres Pasos Formation at Cerro Divisadero, Chile. *Sedimentology* 56, 737–764, doi:10.1111/j.1365-3091.2008.00995.x

Saylor, J. E., and Sundell, K. E. (2016). Quantifying Comparison of Large Detrital Geochronology Data Sets. *Geosphere* 12, 203–220. doi:10.1130/GES01237.1

Schwartz, T. M., Fosdick, J. C., and Graham, S. A. (2017). Using Detrital Zircon U-Pb Ages to Calculate Late Cretaceous Sedimentation Rates in the Magallanes-Austral Basin, Patagonia. *Basin Res.* 29, 725–746. doi:10.1111/bre.12198

Schwartz, T. M., and Graham, S. A. (2015). Stratigraphic Architecture of a Tide-Influenced Shelf-Edge Delta, Upper Cretaceous Dorotea Formation, Magallanes-Austral Basin, Patagonia. *Sedimentology* 62, 1039–1077. doi:10.1111/sed.12176

Selley, R. C. (1968). A Classification of Paleocurrent Models. *J. Geol.* 76, 99–110. doi:10.1086/627311

Sharman, G. R., Graham, S. A., Grove, M., Kimbrough, D. L., and Wright, J. E. (2015). Detrital Zircon Provenance of the Late Cretaceous-Eocene California Forearc: Influence of Laramide Low-Angle Subduction on Sediment Dispersal and Paleogeography. *Geol. Soc. Am. Bull.* 127, 38–60. doi:10.1130/B31065.1

Sharman, G. R., and Malkowski, M. A. (2020). Needles in a Haystack: Detrital Zircon U-Pb Ages and the Maximum Depositional Age of Modern Global Sediment. *Earth-Science Rev.* 203, 103109. doi:10.1016/j.earscirev.2020.103109

Sharman, G. R., Sharman, J. P., and Sylvester, Z. (2018). detritalPy: A Python-Based Toolset for Visualizing and Analysing Detrital Geo-Thermochronologic Data. *Depos. Rec.* 4, 202–215. doi:10.1002/DEP2.45

Shultz, M. R., Fildani, A., Cope, T. D., and Graham, S. A. (2005). Deposition and Stratigraphic Architecture of an Outcropping Ancient Slope System: Tres Pasos Formation, Magallanes Basin, Southern Chile. *Geol. Soc. Lond. Spec. Publ.* 244, 27–50. doi:10.1144/GSL.SP.2005.244.01.03

Sickmann, Z. T., Schwartz, T. M., and Graham, S. A. (2018). Refining Stratigraphy and Tectonic History Using Detrital Zircon Maximum Depositional Age: An Example from the Cerro Fortaleza Formation, Austral Basin, Southern Patagonia. *Basin Res.* 30, 708–729. doi:10.1111/bre.12272

Sickmann, Z. T., Schwartz, T. M., Malkowski, M. A., Dobbs, S. C., and Graham, S. A. (2019). Interpreting Large Detrital Geochronology Data Sets in Retroarc Foreland Basins: An Example from the Magallanes-Austral Basin, Southernmost Patagonia. *Lithosphere* 11, 620–642. doi:10.1130/L1060.1

Sláma, J., Košler, J., Condon, D. J., Crowley, J. L., Gerdes, A., Hanchar, J. M., et al. (2008). Plešovice Zircon - A New Natural Reference Material for U-Pb and Hf Isotopic Microanalysis. *Chem. Geol.* 249, 1–35. doi:10.1016/J.CHEMGEO.2007.11.005

Snedden, J. W., and Dalrymple, R. W. (1999). Modern Shelf Sand Ridges: From Historical Perspective to a Unified Hydrodynamic and Evolutionary Model. *SEPM Spec. Publ. Isol. Shallow Mar. Sand Bodies* 13, 13–28. doi:10.2110/PEC.99.64.0013

Stern, C. R., and de Wit, M. J. (2003). Rocas Verdes Ophiolites, Southernmost South America: Remnants of Progressive Stages of Development of Oceanic-type Crust in a Continental Margin Back-Arc Basin. *Geol. Soc. Lond. Spec. Publ.* 218, 665–683. doi:10.1144/GSL.SP.2003.218.01.32

Suárez, R. J., Ghiglione, M. C., Calderón, M., Sue, C., Martinod, J., Guillaume, B., and Rojo, D. (2019). The Metamorphic Rocks of the Nunatak Viedma in the Southern Patagonian Andes: Provenance Sources and Implications for the Early Mesozoic Patagonia-Antarctic Peninsula Connection. *J. South Am. Earth Sci.* 90, 471–486. doi:10.1016/j.jsames.2018.12.015

Taylor, A. M., and Goldring, R. (1993). Description and Analysis of Bioturbation and Ichnofabric. *J. Geol. Soc. Lond.* 150, 141–148. Available at: http://jgs.lyellcollection.org/. doi:10.1144/gsjgs.150.1.0141

Vermeesch, P. (2018). Dissimilarity Measures in Detrital Geochronology. *Earth-Science Rev.* 178, 310–321. doi:10.1016/J.EARSCIREV.2017.11.027

Vermeesch, P. (2013). Multi-Sample Comparison of Detrital Age Distributions. *Chem. Geol.* 341, 140–146. doi:10.1016/j.chemgeo.2013.01.010

Wilson, T. J. (1991). Transition from Back-Arc to Foreland Basin Development in the Southernmost Andes: Stratigraphic Record from the Ultima Esperanza District, Chile. *Geol. Soc. Am. Bull.* 103, 98–111. Available at: http://pubs.geoscienceworld.org/gsa/gsabulletin/article-pdf/103/1/98/3381166/i0016-7606-103-1-98.pdf. doi:10.1130/0016-7606(1991)103<0098:tfbatf>2.3.co;2

Conflict of Interest: The authors declare that the research was conducted in the absence of any commercial or financial relationships that could be construed as a potential conflict of interest.

Publisher's Note: All claims expressed in this article are solely those of the authors and do not necessarily represent those of their affiliated organizations, or those of the publisher, the editors and the reviewers. Any product that may be evaluated in this article, or claim that may be made by its manufacturer, is not guaranteed or endorsed by the publisher.